

Abstract

Fluid-fault interactions result in many two-way coupled processes across a range of length scales, from the micron scale of the shear zone to the kilometer scale of the slip patch. The scale separation and complex coupling render fluid-fault interactions challenging to simulate and may ultimately limit our understanding of experimental data and induced seismicity. Here we present spectral boundary-integral solutions for in-plane interface sliding and opening in a poroelastic solid. We solve for fault slip in the presence of rate- and state frictional properties, inelastic dilatancy, injection, and the coupling of a shear zone and a diffusive poroelastic bulk. The shear localization zone is treated as having a finite-width and non-constant pore pressure, albeit with a simplified mathematical representation. The dimension of the 2D plane strain problem is reduced to a 1D problem resulting in increased computational efficiency and incorporation of small-scale shear-zone physics into the boundary conditions. We apply the method to data from a fault injection experiment that has been previously studied with modeling. We explore the influence of inelastic dilatancy, bulk poroelastic response, and bulk diffusivity on the simulated fault slip due to the injection. Dilatancy not only alters drastically the stability of fault slip but also the nature of pore pressure evolution on the fault, causing significant deviation from the standard square-root-of-time diffusion. More surprisingly, varying the bulk's poroelastic response (by using different values of the undrained Poisson's ratio) and bulk hydraulic diffusivity can be as critical in determining rupture stability as the inelastic dilatancy.

Plain Language Summary

Earthquakes occur on faults deep in the Earth's crust. At this depth, the faults are surrounded by rock and water that fills up pores and fractures in the rock. This water affects how the surrounding crust responds to earthquakes or slip on the faults. Water also plays an important role within the faults since it will decrease or increase the frictional resistance if it causes pressurization or depressurization, respectively. A common cause of pressurization in faults is by an injection of fluid, which is done for many different purposes ranging from geothermal exploitation, carbon sequestration, or wastewater disposal. Here we develop a new efficient method to simulate fault slip and earthquakes in a porous and fluid-filled medium. This allows us to better understand the role of water in earthquake processes, either in the medium surrounding the fault or within

51 the fault. We compare our method to a previously studied experiment where water was
52 injected directly into a fault and slip measured. In addition, we investigate certain phys-
53 ical properties of the porous rock that have not received much attention in the litera-
54 ture. We find that they significantly influence if earthquakes occur due to injection.

55 1 Introduction

56 The role of fluids in seismic and aseismic faulting processes has been of significant
57 interest in the last few years. Mounting evidence indicates that fluids may play an im-
58 portant role in a diverse set of mechanisms that alter fault slip behavior ranging from
59 earthquake triggering to slow slip events.

60 The most prominent example of fluid and fault interactions is the clear link between
61 fluid injection and induced seismicity, as originally pointed out by Raleigh et al. (1976);
62 Hsieh and Bredehoeft (1981) and remains a critical issue (e.g. Ellsworth, 2013). This phe-
63 nomenon has a straightforward mechanical explanation: higher pore pressures, due to
64 injection, reduce the effective normal stress and thus the frictional resistance of the fault.
65 The fault then slips faster and may accelerate the generation of seismic instabilities. This
66 problem has been frequently modeled with a straightforward implementation of one-way
67 coupling of pore pressure and frictional strength where pore pressure perturbations are
68 imposed and slip or number of seismic events are computed. Injection into faults may
69 lead to sustained aseismic transients (e.g. Viesca & Dublanche, 2019; Bhattacharya &
70 Viesca, 2019), which may later become seismic events depending on the frictional prop-
71 erties of the fault (Larochelle et al., 2021a). A more detailed investigation of this prob-
72 lem reveals considerable complexity in pore pressure evolution if heterogeneous perme-
73 ability structures and poroelasticity are considered (e.g. Yehya et al., 2018)

74 The poroelastic properties of the crust have lately been receiving more interest, most
75 prominently as a long-ranging and fast-acting mechanism in which faults can be stressed
76 due to injection or extraction (Segall & Lu, 2015). However, there is also significant lit-
77 erature on the role of poroelasticity in influencing the nucleation or propagation of seis-
78 mic and aseismic ruptures (Rudnicki & Koutsibelas, 1991; Dunham & Rice, 2008; Jha
79 & Juanes, 2014; Heimisson et al., 2019, 2021). An effect of particular importance in re-
80 gard to the influence of poroelasticity is that, during in-plane sliding, compression and
81 dilation of the host rock induces pore pressure change in the shear zone (Heimisson et

82 al., 2019, 2021); this effect is discussed further in section 1.1. Thus the poroelastic re-
 83 sponse of the bulk, induced by an ongoing rupture, may influence the effective normal
 84 stress and hence shear resistance to the rupture, creating a feedback loop. Poroelastic-
 85 ity also influences and introduces a diffusion-dependent time-evolving shear stress on the
 86 fault plane with significant implications for the stability of sliding (Heimisson et al., 2021).

87 Processes other than poroelasticity may change pore pressure in an active shear
 88 zone and affect rupture and instability formation on faults. The generation of aseismic
 89 slip transients on faults is believed to be related to pore fluids. For example, transient
 90 slow slip events (SSEs) in subduction zones are thought to be related to high pore pres-
 91 sure conditions (e.g., Liu & Rice, 2007; Bürgmann, 2018). A primary challenge in ex-
 92 plaining the mechanics of transient slow slip is to understand why it starts, but does not
 93 become an earthquake. One potential mechanism is a geometric restriction, in which the
 94 high-pore-pressure region is large enough to cause slip acceleration, for example, due to
 95 rate-and-state velocity-weakening friction properties, but too small for that slip to be-
 96 come seismic (Liu & Rice, 2005, 2007). Another potential explanation is the change from
 97 velocity-weakening to velocity-strengthening friction with increasing slip rates (Shibazaki
 98 & Shimamoto, 2007; Hawthorne & Rubin, 2013; Leeman et al., 2016). Rate-and-state
 99 faults with velocity-strengthening friction and additional destabilizing effects can also
 100 produce SSEs in models with poroelasticity (Heimisson et al., 2019) and viscoplasticity
 101 (Tong & Lavier, 2018). Inelastic dilatancy of granular fault gouge, which can lead to a
 102 reduction in pore pressure and stabilize fault slip, has been highlighted as a naturally
 103 present fluid-related mechanism that can explain how slow slip transients do not evolve
 104 into seismic events (e.g. Segall & Rice, 1995; Segall et al., 2010). Modeling of fault slip
 105 with inelastic dilatancy can explain many properties of slow slip events, including their
 106 scaling (Dal Zilio et al., 2020).

107 Multiple mechanisms may act at a time. Recently, numerical simulations have started
 108 exploring the simultaneous injection and inelastic dilatancy in a diffusive shear zone (Ciardo
 109 & Lecampion, 2019; Yang & Dunham, 2021). However, these efforts have been limited
 110 to a non-diffusive and elastic bulk. Coupling with a poroelastic bulk introduces another
 111 degree of complexity, where elastic dilation and compression of the bulk generate pore
 112 pressure transients. Further complexity is introduced by field observations indicating that
 113 permeability of the shear zone in a fault core may be very different from the surround-
 114 ing damage zone and host rock (e.g. Wibberley & Shimamoto, 2003). Further, the shear-

115 ing of gouge material can dramatically reduce the permeability perpendicular to the shear-
116 ing direction and thus result in the shear zone having a significantly anisotropic perme-
117 ability (Zhang et al., 1999).

118 Here we present a spectral boundary-integral method that allows us to simulate
119 quasi-dynamic slow and fast slip on a rate-and-state fault with dilatancy/compaction
120 and fluid flow in a plane-strain poroelastic medium. We take a boundary layer approach
121 where the outer solution, which is the spectral representation of the poroelastic bulk, treats
122 the fault as a zero-thickness interface with suitable boundary conditions. However, the
123 inner solution considers the fault to be a finite-width shear zone. We consider the fric-
124 tional properties of the shear zone to be determined by its width-averaged properties.
125 The bulk is an isotropic standard quasi-static Biot poroelastic solid with a hydraulic dif-
126 fusivity c . The shear zone has frictional strength described by rate-and-state friction, with
127 inelastic state-dependent dilatancy and compaction and anisotropic permeability: the
128 permeability across the shear zone is different than the permeability along the shear zone.
129 The inelastic state-dependent dilatancy and compaction are implemented using the Segall
130 and Rice (1995) approach, as explained later. We frequently refer to this process only
131 as "dilatancy" for the sake of brevity, and that is also how it is commonly referred to
132 in the fault mechanics community. However, we remind the reader that the "dilatancy"
133 law also predicts compaction under certain conditions. The pore pressure in the layer
134 is simplified and assumed to be bi-linear where the two linear profiles are continuous at
135 the center of the shear zone (as in Heimisson et al., 2021, see also section 1.1). The spec-
136 tral representation uses analytical convolution kernels, which are truncated for efficiency
137 similar to Lapusta et al. (2000), but at time scales relevant for the bulk diffusion at the
138 specific wavenumber.

139 When slip speed becomes high enough in a narrow enough shear layer with small
140 enough permeability, then thermal pressurization of pore fluids due to shear heating may
141 also become important (e.g. Rice, 2006; Bizzarri & Cocco, 2006). While such effects may
142 be critical for seismic rupture evolution (e.g. Noda & Lapusta, 2013), they may be neg-
143 ligible or at least much less pronounced in the nucleation phases of the seismic cycle (Segall
144 & Rice, 2006; Segall, 2010), which are primarily the focus of this study. Consequently,
145 we do not account for thermal pressurization.

146 The paper first discusses the general problem setup (section 1.1). For complete-
 147 ness, there is a quick review of governing equations and boundary conditions (section
 148 2). However, we highlight that a more complete description is found in Heimisson et al.
 149 (2021) with the exception of added complexity introduced into the fluid mass balance
 150 (section 2.3.1) not included in previous work. In section 3, we provide the analytical spec-
 151 tral boundary-integral solutions for sliding and opening of an interface in a plane-strain
 152 poroelastic solid. The numerical approach taken to solve the coupled problem - with di-
 153 latancy, compaction, and injection in a poroelastic solid - is described in section 4. Fi-
 154 nally, we show an application of the method (section 5), where we use constraints from
 155 a field experiment (Guglielmi et al., 2015) and a recent numerical study that modeled
 156 the field experiment data (Larochelle et al., 2021a). Finally, we discuss the role of poroe-
 157 lasticity, and other fluid-based mechanisms, in the dynamics of injection-induced seis-
 158 mic and aseismic slip.

159 1.1 Problem description

160 The general problem setup can be divided into three domains. Two are isotropic
 161 poroelastic half-spaces, which we call the bulk, one in $y > 0$ region and the other in $y <$
 162 0 region. The third is a shear zone made from fault gouge, which separates the two half-
 163 spaces (Figure 1a). The two poroelastic half-spaces are assumed to have the same ma-
 164 terial properties, which we characterize through the shear modulus G , Skempton’s co-
 165 efficient B , drained Poisson’s ratio ν , undrained Poisson’s ratio ν_u , and hydraulic dif-
 166 fusivity c (e.g., Cheng, 2016; Detournay & Cheng, 1995; Rice & Cleary, 1976). In some
 167 cases, other poroelastic parameters may be displayed for compactness, legibility, and in-
 168 tuition. However, the implementation of the method we present uses the aforementioned
 169 five.

170 The shear zone is a thin layer of half-width ϵ . Here thin indicates that ϵ should be
 171 much smaller than any significant variation in fields, such as slip or pressure, along the
 172 x -axis, which is fundamental for accuracy of the boundary-layer treatment of the shear
 173 zone. The properties of the shear zone or fault gouge are characterized by reference poros-
 174 ity ϕ_0 , inelastic dilatancy coefficient γ (Segall & Rice, 1995), and pore-pressure and normal-
 175 stress dependent void-volume compressibilities β_n^p and β_n^σ . In addition, the intact gouge
 176 material compressibilities are β_g^p and β_g^σ , and the fluid compressibilities are β_f^p and β_f^σ .
 177 The frictional strength of the shear zone is determined by the reference coefficient of fric-

178 tion f_0 , the characteristic state evolution distance L , the constitutive parameter a that
 179 scales the direct rate dependence of friction, and the constitutive parameter b that scales
 180 the state dependence of friction. These parameters and properties of the shear zone are
 181 the same as in Heimisson et al. (2021) where a more detailed discussion is offered. We
 182 also note that their meaning is presented in the context of the governing equations in
 183 section 2. The hydraulic properties of the layer are somewhat different here compared
 184 to Heimisson et al. (2021). First, we consider that there may be a source of fluid mass
 185 in the layer, for example by injection, indicated by Q . Second, we include an anisotropic
 186 mobility (permeability over dynamic fluid viscosity). In particular, the mobility in the
 187 y direction, κ_{cy} can be different from the mobility in the x direction κ_{cx} . Thus, fluids
 188 injected into the fault have multiple migration paths, along the shear zone, perpendic-
 189 ular to the shear zone, and in both x and y directions in the bulk. Furthermore, an in-
 190 crease in pore pressure in the bulk can migrate into the shear zone and also into the bulk
 191 on the other side. (Figure 1a)

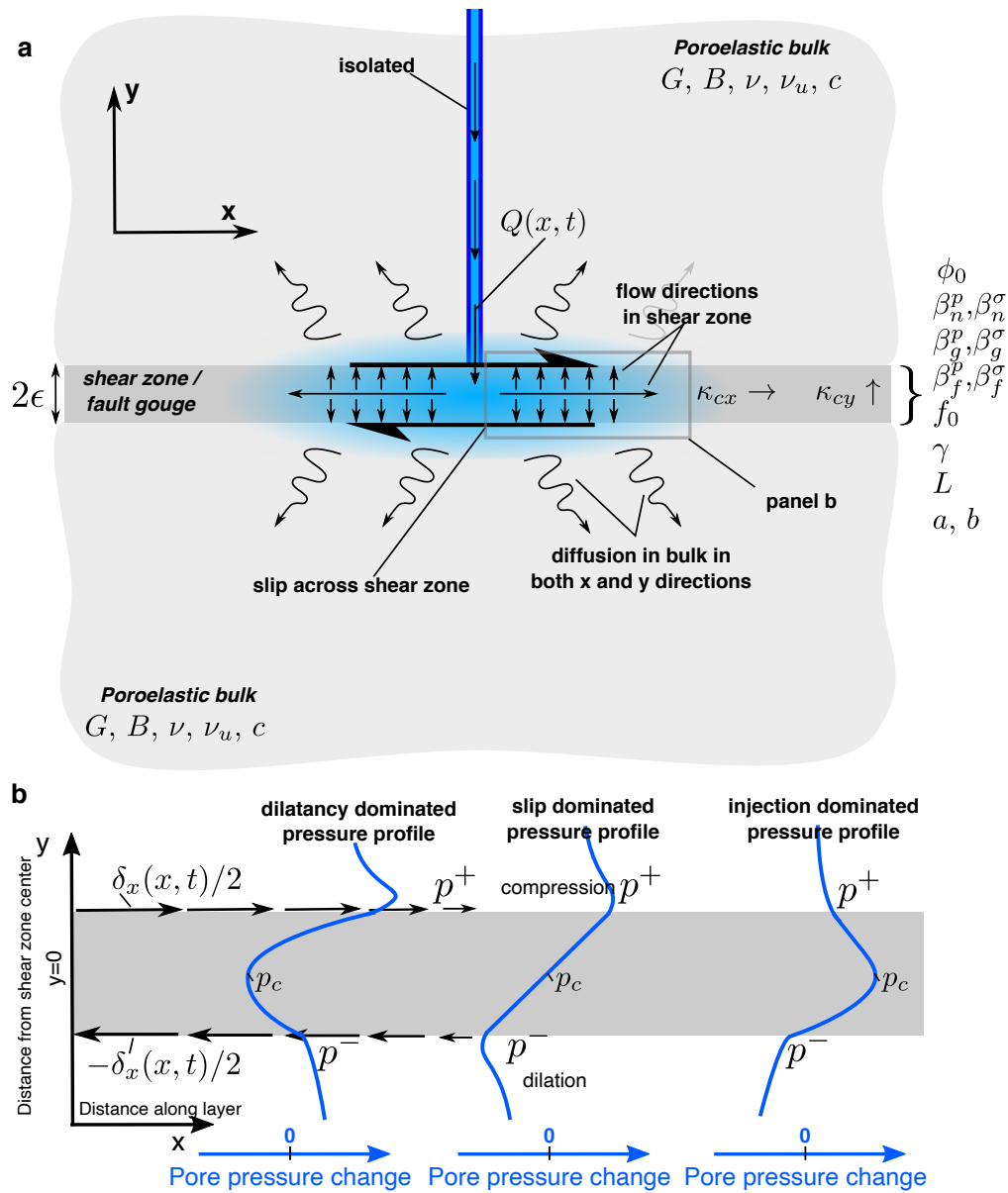


Figure 1. Schematic overview of the problems setup and possible pore pressure profiles scenarios in the shear zone. **a** Injection occurs in a thin shear zone embedded between two poroelastic solids of the same properties. This injection causes fluid migration along the shear zone, across the shear zone, and into the bulk. The evolving pore fluid pressure leads to slip across the shear zone. **b** Pore pressure profiles that can occur during the propagation of a single rupture induced by injection. If the pore pressure diffusion is ahead of the rupture, then the shear zone has increased pressure at the center p_c (right-most profile). Once considerable slip has occurred the inelastic dilatancy may have reduced the pressure, even to the point of being less than hydrostatic, which we may call a dilatancy dominated pore pressure (left-most profile). Between the two cases of an injection dominated regime and a dilatancy dominated regime we expect at or near the rupture tip the two effects may cancel. However, the compression and dilation of the host rock induced by the inhomogeneous slip can significantly change the pore pressures on either side of the shear zone (p^+ and p^-).

192 A key question in induced seismicity is to understand when so-called runaway rup-
 193 tures happen, that is ruptures that propagate well outside a pressurized region. This is
 194 a useful focal point to explain some of the general dynamics that we expect from the de-
 195 scribed problem above. When injection into a fault occurs, there are two important length
 196 scales along the x dimension (Figure 1) that can interact and explain the dynamics of
 197 the slip. First, how far the pressure front from the injection site has diffused, which we
 198 can define as the region of significantly elevated pore pressure. Second, how far the rup-
 199 ture tip has propagated, which can be understood as the region of significant fault slip.
 200 If a fault has relatively low shear stress, i.e., its shear stress over initial effective normal
 201 stress is significantly below its reference friction coefficient, or is well-healed, which may
 202 be common in injection experiments, the pore pressure front controls how far the rup-
 203 ture tip can move since the frictional resistance is too great outside the pressure front
 204 (e.g., Larochelle et al., 2021a). However, if a fault is relatively well-stressed, or if the slip-
 205 ping region enters a more well-stressed portion of the fault or a portion of the fault with
 206 lower friction, then the rupture may become self-sustained and rupture outside the pres-
 207 sure front. Thus the rupture may initially be contained by the pressure front, but evolve
 208 to become a runaway rupture.

209 The interplay of the rupture tip and pressure front provides a useful qualitative ex-
 210 planation of the transition from a confined to runaway rupture. However, additional com-
 211 plexity, which is related to the pressure profile across the fault, plays an important role
 212 in determining the if, when or how such a rupture can happen. If a rupture is initiated
 213 in a shear zone by injection, the pressure profile across the shear zone (i.e. pressure change
 214 with y , Figure 1b) can be dominated by different mechanisms depending on whether ob-
 215 serving the profile at a x coordinate that is ahead of the rupture, at the tip or behind
 216 the tip (Figure 1b). This will be particularly prominent for an in-plane rupture direc-
 217 tion due to the volumetric straining of the bulk. If the pressurized zone is ahead of the
 218 rupture the shear zone central pressure (p_c) will be elevated. The pore pressures adja-
 219 cent to the shear zone (p^+ and p^-) will also be elevated due to the leak-off into the bulk.
 220 Near the tip region, the influence of dilatancy has started to lower the pore pressure p_c ,
 221 but furthermore volumetric straining of the bulk has caused an increase in pore pressure
 222 on the compressive side (p^+) and decrease on the dilating side (p^-) due to poroelastic
 223 coupling. Finally, behind the tip dilatancy may have further reduced the pressure p_c and
 224 possibly reversed the sign compared to the background equilibrium pressure and caused

225 flow back into the shear zone. We thus suggest that in order to model rupture propa-
 226 gation, earthquake nucleation, and understand runaway ruptures in a fluid-saturated medium
 227 due to injection, we must consider coupling that arises from the interplay of several mech-
 228 anisms that alter the pore pressure.

229 **2 Governing equations**

230 This section will describe the conservation laws, friction laws, and boundary con-
 231 ditions. All the governing equations and boundary conditions with the exception of Sec-
 232 tion 2.3.1, which describes the fluid mass balance, are the same as in Heimisson et al.
 233 (2021). We state the equation with brief explanations for completeness, but refer the reader
 234 to Heimisson et al. (2021) for more elaborate discussion and derivations.

235 **2.1 Poroelastic Bulk**

236 The quasi-static theory of poroelasticity can be described as four coupled partial
 237 differential equations written in terms of displacements u_i and pressure changes p rel-
 238 ative to an equilibrium pressure state (e.g., Detournay & Cheng, 1995; Cheng, 2016)

$$Gu_{i,kk} + \frac{G}{1-2\nu}u_{k,ki} = \alpha p_{,i} \quad (1)$$

239 and

$$\frac{1}{M}p_{,t} - \kappa p_{,kk} = -\alpha u_{k,kt}, \quad (2)$$

240 where the material parameters are as follows: G : shear modulus, ν : drained Poisson's
 241 ratio, α : Biot-Willis parameter, M : Biot modulus, and κ is the mobility (the ratio be-
 242 tween the permeability and fluid viscosity). In later expressions a different set of poroe-
 243 lastic material parameter may be used for compactness and increased intuition.

244 In this work, we assume plane strain deformation, in which case the governing equa-
 245 tions can be reduced to three. Further simplification and decoupling of the governing equa-
 246 tions is possible by using the McNamee-Gibson displacement functions (McNamee & Gib-
 247 son, 1960; Verruijt, 1971). In obtaining solutions to equations (1) and (2) we follow the
 248 strategy explained in the Appendix of Heimisson et al. (2019) using the McNamee-Gibson
 249 displacement functions but using the boundary conditions listed in the next section.

250 **2.1.1 Boundary conditions**

251 Here we apply the same boundary conditions as in (Heimisson et al., 2021) at the
 252 interface, i.e. the shear zone and at infinity.

$$\lim_{y \rightarrow 0^\pm} u_x^+ - u_x^- = \delta_x, \tag{3}$$

$$\lim_{y \rightarrow 0^\pm} u_y^+ - u_y^- = \delta_y, \tag{4}$$

$$\lim_{y \rightarrow \pm\infty} u_x^\pm = 0 \text{ and } u_y^\pm = 0, \tag{5}$$

$$\lim_{y \rightarrow \pm\infty} p^\pm = 0, \tag{6}$$

$$\lim_{y \rightarrow 0^\pm} \sigma_{xy}^+ - \sigma_{xy}^- = 0, \tag{7}$$

$$\lim_{y \rightarrow 0^\pm} \sigma_{yy}^+ - \sigma_{yy}^- = 0, \tag{8}$$

253 where we have dropped the index notation and used x and y (as represented in Figure
 254 1a).

255 The pore pressure in the shear zone is assumed to be bi-linear as in Heimisson et
 256 al. (2021) This is a generalization of the leaky interface used in the plane strain dislo-
 257 cation solution of Song and Rudnicki (2017). The pore pressure across the shear zone
 258 is parameterized in terms of pressure at the center p_c at $y = 0$ and the pressure at the
 259 shear zone boundaries where the poroelastic bulk meets the shear zone, that is, p^\pm at
 260 $y = \epsilon^\pm$. We can explicitly write out the assumed pore pressure profile as:

$$\begin{aligned} p(y) &= \frac{y}{\epsilon}(p^+ - p_c) + p_c \quad \text{if } 0 < y < \epsilon \\ p(y) &= \frac{y}{\epsilon}(p_c - p^-) + p_c \quad \text{if } -\epsilon < y < 0. \end{aligned} \tag{9}$$

261 Thus equating the fluid mass flux into the shear zone and in the the bulk, and vice versa,
 262 gives rise to a pressure gradient boundary condition:

$$\left. \frac{dp^\pm}{dy} \right|_{y=0^\pm} = \pm \frac{\kappa_{cy}}{\kappa} \frac{(p^\pm - p_c)}{\epsilon}, \tag{10}$$

263 where κ_{cy} is the shear zone mobility in the y direction and κ is the poroelastic bulk mo-
 264 bility which is rated to the bulk hydraulic diffusivity by $c = M\kappa$. We note that bound-
 265 ary conditions for the bulk are applied at $y = 0^\pm$ but in the description of the shear

266 zone we treat it as a finite layer with thickness between $y = \pm\epsilon$. This is because we take
 267 a boundary layer approach (similar to Appendix B of Rudnicki & Rice, 2006) where the
 268 inner solution, the shear zone, is assumed to have a finite thickness. However, the outer
 269 solution, the bulk, approximates the layer as having an infinitesimal thickness. Thus the
 270 assumption that any variation along the length of the shear zone occurs over a length
 271 scale much smaller than ϵ is implicit. In other words, we always require that $\epsilon k \ll 1$,
 272 with k representing the wavenumber (inverse of a wavelength) of any field that varies
 273 along the x -dimension.

274 2.2 Frictional properties

275 As in Heimisson et al. (2021) we represent the frictional strength of the layer in an
 276 averaged sense.

277 Let us assume that the frictional strength of every point in the layer can be rep-
 278 resented as follows:

$$\frac{\tau(x, t)}{\sigma(x, t) - p(x, y, t)} = f(x, y, t) \quad \text{for } -\epsilon < y < \epsilon, \quad (11)$$

279 where $\tau(x, t)$ is the sum of all contributions to the shear stress, both initial background
 280 value and slip contributions. We note that the shear stress is assumed to be spatially con-
 281 stant across the layer. Similarly, $\sigma(x, t)$ represents background initial effective normal
 282 stress (normal stress minus the ambient pore pressure) in addition to the slip induced
 283 changes in normal stress and we assume is spatially constant across the layer. However,
 284 we have separated from the description the perturbations in pore pressure $p(x, y, t)$ since,
 285 as previously discussed, they cannot be assumed to be constant in y . Using equation (9)
 286 and averaging over the layer, we obtain:

$$\tau \frac{(p_c - p^+) \log\left(\frac{\sigma - p^-}{\sigma - p_c}\right) + (p_c - p^-) \log\left(\frac{\sigma - p^+}{\sigma - p_c}\right)}{2(p_c - p^-)(p_c - p^+)} = \langle f \rangle, \quad (12)$$

287 with the $\langle f \rangle$ representing the frictional coefficient of the layer. We have explored using
 288 the equation above for modeling the interface frictional strength, but we find that it ren-
 289 ders very similar results as an linearized approximation valid in the limit of the pore pres-
 290 sure changes being small compared to the background normal stress:

$$\tau = (\sigma - \langle p(t) \rangle) \langle f \rangle, \quad (13)$$

291 where $\langle p(t) \rangle$ is the average pressure across the layers and can be computed directly

$$\langle p \rangle = \frac{1}{2\epsilon} \int_{-\epsilon}^{\epsilon} p(y) dy = \frac{1}{2} \left(p_c + \frac{p^+ + p^-}{2} \right). \quad (14)$$

292 Equation (13) further offers a simpler interpretation of the role of the pore pressure in
 293 the effective normal stress compared to equation (12), which helps in understanding the
 294 simulation results.

295 We interpret the averaged friction coefficient $\langle f \rangle$ of the shear zone as being rep-
 296 resented by the rate-and-state friction law (e.g., Dieterich, 1979; Ruina, 1983; Marone,
 297 1998):

$$\langle f \rangle = \frac{1}{2\epsilon} \int_{-\epsilon}^{\epsilon} f(x, y, t) dy = a \operatorname{arcsinh} \left[\frac{V}{2V_0} \exp \left(\frac{f_0 + b \log(V_0 \theta / L)}{a} \right) \right], \quad (15)$$

298 where we use the regularized form of the friction law that is also valid for slip speeds V
 299 much smaller than the reference slip speed V_0 (Rice & Ben-Zion, 1996; Ben-Zion & Rice,
 300 1997; Lapusta et al., 2000). Here a and b are constitutive parameters that describe the
 301 rate dependence and state dependence of friction, respectively. Further, f_0 is the refer-
 302 ence coefficient and L is the characteristic slip distance over which the state evolves. The
 303 state variable is described by the aging law (Ruina, 1983):

$$\frac{d\theta}{dt} = 1 - \frac{\theta V}{L} \quad (16)$$

304 We note that here we have introduced a minor difference compared to (Heimisson
 305 et al., 2021). We represent friction using the regularized friction law whereas the non-
 306 regularized version was discussed by (Heimisson et al., 2021). In the linearized analy-
 307 sis treated by Heimisson et al. (2021), there is no difference between the two versions.

308 **2.3 Shear Zone**

309 Here we analyze the fluid and solid constituent mass balance of the shear zone gouge.
 310 This analysis is largely based on Heimisson et al. (2021) although here we introduce new
 311 physical processes into fluid mass balance, which are detailed below. Heimisson et al. (2021)

312 linearized all relations around steady-state sliding, which is needed for the purpose of
 313 linearized stability analysis. While not strictly needed for a numerical algorithm, we will
 314 here also linearize and neglect non-linear terms that arise for various reasons. Firstly,
 315 this is done because we have adapted linear compressibility relationships, as is commonly
 316 done, for the fluid, solid and pore-space. Thus for consistency, all terms should be lin-
 317 earized. Second, some non-linear terms have a ϵk scaling, which is by definition a small
 318 parameter. Third, since we adopt a boundary layer treatment of the shear zone with av-
 319 eraging in y over the thickness of the layer, the non-linearity prevents such averaging from
 320 being carried out analytically and largely negates the computational benefits from the
 321 boundary layer treatment.

322 **2.3.1 Fluid mass balance**

323 While other governing equations presented here are identical to those derived and
 324 used by Heimissson et al. (2021), we will introduce two additional physical processes to
 325 the fluid mass balance of the shear zone. We will thus re-derive the fluid mass balance.
 326 The two processes incorporate an injection or source term and allow for along shear zone
 327 lateral diffusion.

328 Within the shear zone, we state the fluid mass balance:

$$\frac{\partial m}{\partial t} + \frac{\partial q_y}{\partial y} + \frac{\partial q_x}{\partial x} = \frac{\partial}{\partial t}(Q(x, t)), \quad (17)$$

329 where m is the fluid mass content and q_y is fluid mass flux perpendicular to the fault (y-
 330 axis) and q_x is the fluid mass flux parallel to the fault (x-axis). $Q(x, t)$ is the cumula-
 331 tive fluid mass injected per unit volume of the shear zone

332 We note that $m = \rho_f n$, where ρ_f is fluid density and $n = n^e + n^p$ is the sum of
 333 elastic and plastic void volume and thus

$$\dot{m} = \dot{\rho}_f n + \rho_f \dot{n}. \quad (18)$$

334 Following Heimissson et al. (2021) we linearize $\dot{n}^e = \phi(\beta_n^p \dot{p} - \beta_n^\sigma \dot{\sigma})$ and $\dot{\rho}_f = \rho_{fo}(\beta_f^p \dot{p} +$
 335 $\beta_f^\sigma \dot{\sigma})$, where β_f^p and β_n^p are fluid and elastic void compressibilities respectively and $\sigma >$
 336 0 means increased compression, also know as “the compression positive” convention. The
 337 reference compressibilities are defined at the reference void volume fraction ϕ and fluid

338 density ρ_{fo} . We assume the reference void volume fraction is the same as the porosity.
 339 Similarly, we assume plastic void fraction is equal to the plastic porosity: $n^{pl} = \phi^{pl}$.
 340 Thus equation (18) becomes:

$$\dot{m} = \rho_{fo}\phi(\beta_f^p \dot{p} + \beta_n^\sigma \dot{\sigma}) + \rho_{fo}\phi(\beta_n^p \dot{p} - \beta_n^\sigma \dot{\sigma} + \dot{\phi}^{pl}/\phi). \quad (19)$$

341 Darcy’s law provides the following linearization:

$$q_x = -\rho_{fo}\kappa_{cx} \frac{\partial p}{\partial x} \quad (20)$$

342 where κ_{cx} is the mobility (permeability over dynamic viscosity) for fluid flux along the
 343 x-axis within the shear zone and is assumed to be spatially constant with respect to x .

344 Combining equations (17), (19), and (20) and integrating with respect to the y-axis
 345 gives

$$2\epsilon\rho_{fo}\phi \left[(\beta_f^p + \beta_n^p)\langle \dot{p} \rangle + (\beta_f^\sigma - \beta_n^\sigma)\dot{\sigma} + \langle \dot{\phi} \rangle^{pl}/\phi \right] + q_y^+ - q_y^- - 2\epsilon\rho_{fo}\kappa_{cx} \frac{\partial^2 \langle p \rangle}{\partial x^2} = 2\epsilon\dot{Q}(x, t) \quad (21)$$

346 where the source terms Q is assumed constant with respect to y .

347 Inserting for the fluid mass flux in y direction given a linear pressure distribution
 348 in the shear zone (equations (10) and (9)) provides:

$$\langle \dot{p} \rangle + \frac{\beta_f^\sigma - \beta_n^\sigma}{\beta_f^p + \beta_n^p} \dot{\sigma} = -\frac{\langle \dot{\phi} \rangle^{pl}}{\phi(\beta_f^p + \beta_n^p)} + \frac{\kappa_{cy}}{\epsilon^2\phi(\beta_f^p + \beta_n^p)} \left(\frac{1}{2}(p^+ + p^-) - p_c \right) + \frac{\kappa_{cx}}{\phi(\beta_f^p + \beta_n^p)} \frac{\partial^2 \langle p \rangle}{\partial x^2} + \frac{\dot{Q}(x, t)}{\rho_{fo}\phi(\beta_f^p + \beta_n^p)}. \quad (22)$$

349 We have thus derived an equation that relates average pressure, normal stress, dilatancy,
 350 along shear zone diffusion, and fluid mass injection. The inelastic changes in porosity
 351 ϕ^{pl} is taken as

$$\langle \phi \rangle^{pl} = \phi_0^{pl} - \gamma \log \left(\frac{V_0 \theta}{L} \right), \quad (23)$$

352 based on Segall and Rice (1995) and Segall et al. (2010), which proposed that the inelas-
 353 tic porosity is a function of the frictional state variable $\phi^{pl}(\theta)$. Recently this idea has gained
 354 more observational support (Proctor et al., 2020). Further, we assume that the frictional
 355 state variable θ describes the average porosity change in the shear layer.

356 Before implementing equation (22) numerically, we analytically integrate to obtain

$$\langle p \rangle + \frac{\beta_f^\sigma - \beta_n^\sigma}{\beta_f^p + \beta_n^p} \sigma = \frac{1}{\phi(\beta_f^p + \beta_n^p)} \left(\frac{Q(x, t)}{\rho_{fo}} - \langle \phi \rangle^{pl} + \int_0^t \frac{\kappa_{cy}}{\epsilon^2} \left(\frac{1}{2}(p^+ + p^-) - p_c \right) + \kappa_{cx} \frac{\partial^2 \langle p \rangle}{\partial x^2} dt' \right), \quad (24)$$

357 where it is assumed that all fields are 0 at $t = 0$

358 **2.3.2 Solid gouge constituent mass balance**

359 We use the same solid constituent mass balance as in Heimisson et al. (2021) to
 360 obtain a constitutive relationship for fault perpendicular displacements:

$$\dot{\delta}_y = 2\epsilon \left(\frac{\phi}{1-\phi} \beta_n^p - \beta_g^p \right) \left[\langle \dot{p} \rangle - \frac{\left(\frac{\phi}{1-\phi} \beta_n^\sigma + \beta_g^\sigma \right)}{\left(\frac{\phi}{1-\phi} \beta_n^p - \beta_g^p \right)} \dot{\sigma} \right] + 2\epsilon \frac{\langle \dot{\phi} \rangle^{pl}}{1-\phi}. \quad (25)$$

361 Assuming that at $t = 0$ the fault is in pressure equilibrium and steady-state sliding, such
 362 that no net dilatancy or compaction occurs, then the equation can be integrated

$$\delta_y = 2\epsilon \left(\frac{\phi}{1-\phi} \beta_n^p - \beta_g^p \right) \left[\langle p \rangle - \frac{\left(\frac{\phi}{1-\phi} \beta_n^\sigma + \beta_g^\sigma \right)}{\left(\frac{\phi}{1-\phi} \beta_n^p - \beta_g^p \right)} \sigma \right] + 2\epsilon \frac{\langle \phi \rangle^{pl}}{1-\phi}. \quad (26)$$

363 **3 Solutions for Coupled Shear Zone and Bulk**

364 In this section we define the joint Fourier-Laplace transform

$$\bar{\hat{\delta}}_x(s, k) = \int_0^\infty \int_{-\infty}^\infty \delta_x(t, x) e^{-ikx-st} dx dt, \quad (27)$$

365 applied here in the slip $\delta_x(x, t)$, or displacement discontinuity across the layer in the x
 366 direction, where the bar symbol represents the Laplace transform in time and the hat
 367 the Fourier transform along the x spatial axis. Some symbols may not carry the hat sym-
 368 bol if they are explicitly written out in term in terms of the wavenumber k .

369 As in Heimisson et al. (2021), we follow the procedure outlined by Heimisson et
 370 al. (2019). In particular, we derive solutions in the Fourier-Laplace domain for shear stress,
 371 pore pressure, and normal stress change at the slip surface ($y \rightarrow 0^\pm$). As provided by
 372 Heimisson et al. (2021) the relationships between change in shear stress $\bar{\hat{\tau}}'$, pore pres-

373 sure change on either side of the layer \bar{p}^\pm , and change in total normal stress $\bar{\sigma}_{yy}$ in terms
 374 of $\bar{\delta}_x$, $\bar{\delta}_y$, and \bar{p}_c are given by the following equations:

$$\bar{\tau} = -\frac{G|k|\bar{\delta}_x}{2(1-\nu_u)}\bar{H}_1(s, k) \quad (28)$$

375 and

$$\bar{p}^\pm = \mp \frac{ikGB\bar{\delta}_x}{3} \frac{1+\nu_u}{1-\nu_u} \bar{H}_2(s, k) - \bar{p}_c \frac{\mathcal{F}}{\mathcal{F}+1} (\bar{H}_2(s, k) - 1) + \frac{|k|GB\bar{\delta}_y}{3} \frac{1+\nu_u}{1-\nu_u} \bar{H}_2(s, k), \quad (29)$$

376 and

$$\bar{\sigma}_{yy} = \bar{p}_c \frac{3}{2B(1+\nu_u)} \frac{\mathcal{F}}{\mathcal{F}+1} (\bar{H}_1(s, k) - 1) - \frac{G|k|\bar{\delta}_y}{2(1-\nu_u)} \bar{H}_1(s, k), \quad (30)$$

377 where

$$\bar{H}_1(s, k) = 1 - \frac{2(\nu_u - \nu) ck^2}{1-\nu} \frac{1+\mathcal{F}}{s} \frac{1}{\mathcal{F} + \sqrt{1+s/ck^2}} \left(\sqrt{1+s/ck^2} - 1 \right), \quad (31)$$

378 and

$$\bar{H}_2(s, k) = \frac{\sqrt{1+s/ck^2} - 1}{\sqrt{1+s/ck^2} + \mathcal{F}}. \quad (32)$$

379 \mathcal{F} is a dimensionless group that characterizes the importance of flux across the fault:

$$\mathcal{F} = \frac{\kappa_{cy}}{\kappa} \frac{1}{|k|\epsilon}. \quad (33)$$

380 We now seek to invert the Laplace transform. We define

$$\bar{K}_1 = \bar{H}_1 - 1 \text{ and } \bar{K}_2 = \bar{H}_2 - 1. \quad (34)$$

381 As was shown by Heimisson et al. (2019), \bar{H}_1 and \bar{H}_2 approach unity in the limit of short
 382 time or negligible diffusion, which reduces Eqs. (28), (29), and (30) to their correspond-
 383 ing undrained limits. \bar{K}_1 and \bar{K}_2 thus represent the transient changes in shear stress and
 384 pore pressure on the fault that arise due to pore pressure diffusion.

385 We note that $\bar{H}_1 = 1 - 2(\nu_u - \nu)/(1 - \nu)(1 + \mathcal{F})(ck^2/s)\bar{H}_2$. Thus in the time do-
 386 main the inverse transform of \bar{H}_1 is closely related to the time integral of the inverse trans-
 387 form of \bar{H}_2 . Using the convolution theorem for Laplace transforms we find that Eqs. (28)
 388 and (29) take the form:

$$\hat{\tau}' = -\frac{G|k|}{2(1 - \nu_u)} \left(\hat{\delta}_x + \int_0^t \hat{\delta}_x(t')K_1(t - t', k)dt' \right), \quad (35)$$

$$\begin{aligned} \hat{p}^\pm = \mp \frac{ikGB}{3} \frac{1 + \nu_u}{1 - \nu_u} \left(\hat{\delta}_x + \int_0^t \hat{\delta}_x(t')K_2(t - t', k)dt' \right) - \frac{\mathcal{F}}{\mathcal{F} + 1} \int_0^t \hat{p}_c(t')K_2(t - t', k)dt' \\ + \frac{|k|GB}{3} \frac{1 + \nu_u}{1 - \nu_u} \left(\hat{\delta}_y + \int_0^t \hat{\delta}_y(t')K_2(t - t', k)dt' \right). \end{aligned} \quad (36)$$

389 and

$$\hat{\sigma}_{yy} = \frac{3}{2B(1 + \nu_u)} \frac{\mathcal{F}}{\mathcal{F} + 1} \int_0^t \hat{p}_c(t')K_1(t - t', k)dt' - \frac{G|k|}{2(1 - \nu_u)} \left(\hat{\delta}_y + \int_0^t \hat{\delta}_y(t')K_1(t - t', k)dt' \right) \quad (37)$$

390 We have thus separated the undrained response and the transient diffusion behav-
 391 ior. This behavior characterized by the convolution kernels K_1 and K_2 that represent
 392 the inverse Laplace transforms of \bar{K}_1 and \bar{K}_2 respectively. In other words $K_1(t) = \mathcal{L}^{-1} \{ \bar{K}_1 \} (t)$
 393 and $K_2(t) = \mathcal{L}^{-1} \{ \bar{K}_2 \} (t)$.

394 Analytical expressions for K_1 and K_2 can be attained through repeated applica-
 395 tion of the convolution theorem to separate \bar{K}_1 and \bar{K}_2 into factors of known inverse Laplace
 396 transforms.

$$K_1(t, k) = -\frac{2(\nu_u - \nu)}{1 - \nu} ck^2(1 + \mathcal{F}) \left(1 + \frac{1}{\mathcal{F} - 1} \left[\mathcal{F}e^{(\mathcal{F}^2 - 1)ck^2t} \operatorname{erfc}(\mathcal{F}\sqrt{ck^2t}) - \mathcal{F} + \operatorname{erf}(\sqrt{ck^2t}) \right] \right) \quad (38)$$

$$K_2(t, k) = -ck^2(1 + \mathcal{F}) \left[\frac{e^{-ck^2t}}{\sqrt{\pi ck^2t}} - \mathcal{F}e^{(\mathcal{F}^2 - 1)ck^2t} \operatorname{erfc}(\mathcal{F}\sqrt{ck^2t}) \right]. \quad (39)$$

397 We note that kernel K_2 is singular when $t \rightarrow 0$. However, this is an integrable singu-
 398 larity and the convolution kernel can be integrated in the sense of taking a Cauchy prin-
 399 cipal value.

400 In summary, equations (35), (36), and (37) represent analytical solutions for the
 401 shear stress, pore pressure (at shear zone boundary), and normal stress given a time-history
 402 of slip δ_x , opening δ_y and/or shear zone center pore pressure p_c which have been trans-
 403 formed in the wavenumber (Fourier) domain. Alternatively, these expressions represent
 404 analytical solutions for a single plane wave perturbation in slip δ_x , δ_y and/or p_c of generic
 405 form $f(t) \exp(ikx)$, where $f(t)$ is some time-dependent function. In section 4.1 we use
 406 this property to construct general solutions for arbitrary histories of slip δ_x , opening δ_y
 407 and/or shear zone center pore pressure p_c .

408 4 Numerical Method

409 4.1 Fourier series representation of poroelastic relations

410 We represent δ_x , δ_y and p_c as a Fourier series

$$\delta_x(x, t) = \sum_{n=-N/2}^{N/2-1} D_{x,n}(t) e^{ik_n x}, \quad k_n = \frac{2\pi n}{\lambda}, \quad (40)$$

$$\delta_y(x, t) = \sum_{n=-N/2}^{N/2-1} D_{y,n}(t) e^{ik_n x}, \quad k_n = \frac{2\pi n}{\lambda}, \quad (41)$$

and

$$p_c(x, t) = \sum_{n=-N/2}^{N/2-1} P_n(t) e^{ik_n x}, \quad k_n = \frac{2\pi n}{\lambda}, \quad (42)$$

411 where N is even and equal to the number of points at which $\delta(x, t)$ and $p_c(x, t)$ are eval-
 412 uated, λ represents the length of the simulation domain. The Fourier transform is given
 413 by

$$\hat{\delta}_x(k, t) = \sum_{n=-N/2}^{N/2-1} 2\pi D_{x,n}(t) \delta_D(k - k_n), \quad (43)$$

414 and corresponding relations exist for \hat{p}_c and $\hat{\delta}_y$ where δ_D is the Dirac delta function. In-
 415 serting the transformed series into equations (35), (36), and (37) and performing the
 416 trivial inverse Fourier transforms provide

$$\tau' = -\frac{G}{2(1-\nu_u)} \sum_{n=-N/2}^{N/2-1} |k_n| \left(D_{x,n}(t) + \int_0^t D_{x,n}(t') K_1(t-t', k_n) dt' \right) e^{ik_n x}, \quad (44)$$

$$\begin{aligned}
 p^\pm = & \sum_{n=-N/2}^{N/2-1} \left(\mp \frac{iGB}{3} \frac{1+\nu_u}{1-\nu_u} k_n \left[D_{x,n}(t) + \int_0^t D_{x,n}(t') K_2(t-t', k_n) dt' \right] + \dots \right. \\
 & \frac{GB}{3} \frac{1+\nu_u}{1-\nu_u} |k_n| \left[D_{y,n}(t) + \int_0^t D_{y,n}(t') K_2(t-t', k_n) dt' \right] - \dots \\
 & \left. \frac{\mathcal{F}(k_n)}{\mathcal{F}(k_n) + 1} \int_0^t P_n(t') K_2(t-t', k_n) dt' \right) e^{ik_n x}, \tag{45}
 \end{aligned}$$

417 and

$$\begin{aligned}
 \sigma_{yy} = & \frac{3}{2B(1+\nu_u)} \sum_{n=-N/2}^{N/2-1} \left(\frac{\mathcal{F}(k_n)}{\mathcal{F}(k_n) + 1} \int_0^t P_n(t') K_1(t-t', k_n) dt' - \dots \right. \\
 & \left. \frac{G}{2(1-\nu_u)} |k_n| \left[D_{y,n}(t) + \int_0^t D_{y,n}(t') K_1(t-t', k_n) dt' \right] \right) e^{ik_n x} \tag{46}
 \end{aligned}$$

418 Testing and validation revealed that the first term of the pore pressure (Eq. 45)
 419 is prone to developing the Gibbs phenomenon in the presence of steep gradients. This
 420 may stem from how the sign of the pore pressure depends on k_n and not the absolute
 421 value of $|k_n|$ as for other terms. Oscillations, such as the Gibbs phenomena, are some-
 422 what mitigated by the diffusional nature of the pore pressure where short-wavelength
 423 oscillations diffuse rapidly. However, a much improved convergence of the series in Eq.
 424 (29) and nearly complete removal of the Gibbs phenomenon can be achieved with a Lanc-
 425 zos sigma factor (Duchon, 1979):

$$\begin{aligned}
 p^\pm = & \sum_{n=-N/2}^{N/2-1} \left(\mp \frac{iGB}{3} \frac{1+\nu_u}{1-\nu_u} k_n \operatorname{sinc} \left(\frac{n}{N/2} \right) \left[D_{x,n}(t) + \int_0^t D_{x,n}(t') K_2(t-t', k_n) dt' \right] + \dots \right. \\
 & \frac{GB}{3} \frac{1+\nu_u}{1-\nu_u} |k_n| \left[D_{y,n}(t) + \int_0^t D_{y,n}(t') K_2(t-t', k_n) dt' \right] - \dots \\
 & \left. \frac{\mathcal{F}(k_n)}{\mathcal{F}(k_n) + 1} \int_0^t P_n(t') K_2(t-t', k_n) dt' \right) e^{ik_n x}, \tag{47}
 \end{aligned}$$

426 where $\operatorname{sinc}(x) = \sin(\pi x)/(\pi x)$ is the normalized sinc function. It is worth noting that
 427 an inverse FFT of the Fourier coefficients in equations 44, 45, 46, and 47 is an efficient
 428 way to compute the stresses and pore pressure at each value of x .

429 **4.1.1 Comparison to Song and Rudnicki (2017)**

430 To partially validate solutions in the previous section we compare to the analyt-
 431 ical solution provided for a single edge dislocation on a leaky plane provided by Song and

432 Rudnicki (2017) (Figure 2). In the problem analyzed by Song and Rudnicki (2017) $\delta_x =$
 433 $\mathcal{H}(t)\mathcal{H}(-x)$, $\delta_y = 0$, $p_c = 0$, in which case $\sigma_{yy} = 0$. We use equations (44) and (47)
 434 after retrieving Fourier series coefficients using a fast Fourier transform (FFT) algorithm
 435 of $\delta_x = \mathcal{H}(t)\mathcal{H}(-x)$ evaluated on a domain size ranging from $x = -50$ to $x = 50$ m.
 436 Comparison in Figure 2 reveals excellent agreement between the two approaches.

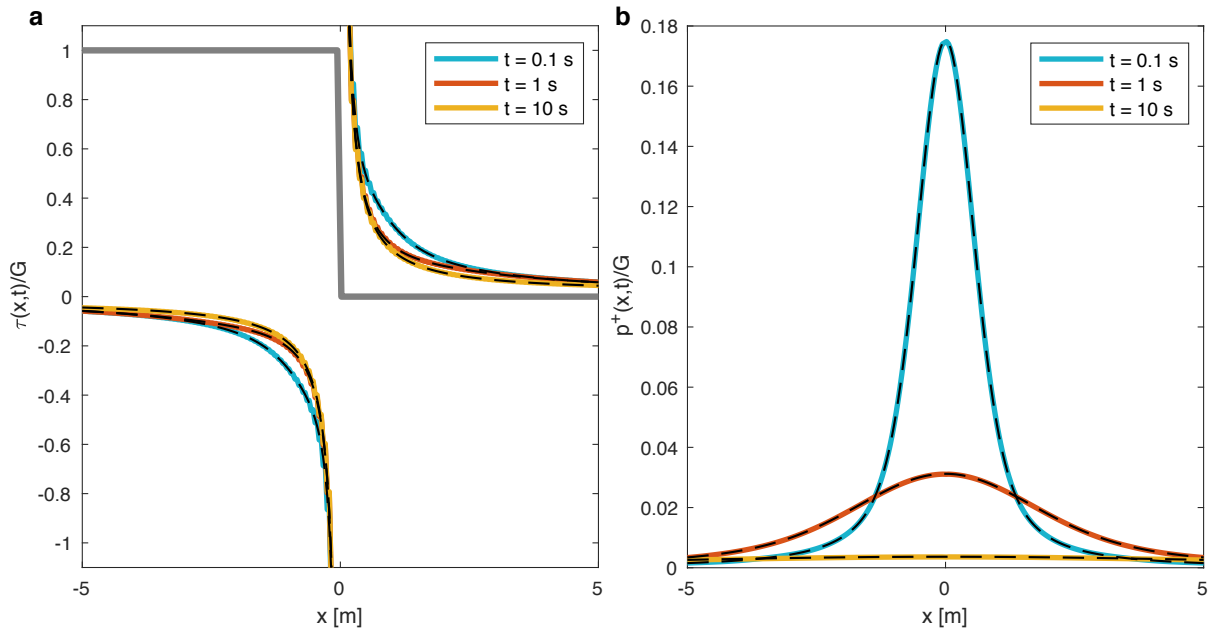


Figure 2. Comparison of equations (44) and (47) to equations (A1) and (72) respectively in Song and Rudnicki (2017). Colored lines represent the spectral boundar-integral solution and overlapping dashed black lines represent the Song and Rudnicki (2017) solution. **a** Shear stress normalized by shear modulus G near the dislocation edge (indicated in gray) of unit slip amplitude at three different times, which span approximately the undrained, drained limits as well as an intermediate stage. **b** pore pressure due to the same edge dislocation. Results are shown for $c = 1 \text{ m}^2/\text{s}$, $B = 0.5$, $\kappa_c/(\kappa\epsilon) = 1 \text{ m}^{-1}$, $\nu = 0.15$, $\nu_u = 0.45$.

437 **4.2 Time-stepping**

438 Here we describe the time-stepping scheme to simulate slow and fast slip with di-
 439 latancy and fluid injection into the faults. The scheme builds on the predictor-corrector
 440 schemes of Lapusta et al. (2000) and Heimissson (2020). However, several significant mod-
 441 ifications have been introduced to resolve fluid diffusion. Below we shall describe the stages

442 of a single time-step by the algorithm. We also refer the reader to the source code (Heimisson,
443 2022) for a more explicit implementation of the time-stepping scheme.

- 444 1. Initial explicit Euler prediction is made for time $t^{n+1} = t^n + \Delta t$ for δ_x^* , δ_y^* , p_c^* ,
445 V^* , where the asterisk represents the prediction of the next time-step.
- 446 2. Fourier coefficients are computed corresponding to the prediction values δ_x^* , δ_y^* ,
447 p_c^* , that is $D_{x,n}^*$, $D_{y,n}^*$, P_n^* using a Fast-Fourier Transform (FFT).
- 448 3. Using equations (44), (46), and (47) the Fourier coefficients for changes in shear
449 stress, normal stress and boundary pore pressure are computed and an inverse FFT
450 is used to sum all Fourier modes.
- 451 4. Prediction for shear stress τ^* and effective normal stress $(\sigma - p)^*$ is computed.
452 In the results, we use the average pore pressure $\langle p \rangle$; however, we note that p could
453 here represent any number of pore pressure values, e.g. p^\pm or p_c , depending on
454 what assumptions are made about the relevant pore pressure in the shear local-
455 ization region. In our numerical implementation (Heimisson, 2022), the user sets
456 which pore pressure to use.
- 457 5. Prediction of the updated state-variable is computed using the analytical integra-
458 tion of the aging law by Kaneko et al. (2011) which is assumes constant slip speed
459 from t to $t + \Delta t$

$$\theta^* = \theta^p \exp\left(-\frac{\Delta t}{2L}(V^n + V^*)\right) + \frac{2L}{(V^n + V^*)} \left(1 - \exp\left(-\frac{\Delta t}{2L}(V^n + V^*)\right)\right), \quad (48)$$

460 where we have taken taken the slip speed as the average $(V^p + V^*)/2$ between
461 the slip speed at time t^n and $t^{n+1} = t^n + \Delta t$. Here we use the superscript n to
462 represent the fields at the previous time step, that is at time t^n .

6. Via an algebraic manipulation of the rate-and-state friction law (13) and (15) a
correction for the slip speed is computed

$$V^{**} = 2V_0 \sinh\left(\frac{\tau^* - \eta V^*}{a(\sigma - p)^*} \exp\left(-f_0/a - \frac{b}{a} \log(V_0 \theta^*/L)\right)\right). \quad (49)$$

463 However, for locations along the fault where the slip speed exceeds a threshold value
464 (here set to 1 cm/s) the previous expression is found to lead to numerical disper-
465 sion and the slip speed is obtained by solving the following non-linear equation
466 as done by Heimisson (2020):

$$\left| V^{**} - 2V_0 \sinh \left(\frac{\tau^* - \eta V^*}{a(\sigma - p)^*} \exp \left(-f_0/a - \frac{b}{a} \log(V_0 \theta^*/L) \right) \right) \right| = 0. \quad (50)$$

467 7. Using the new slip speed correction V^{**} the state variable is also updated

$$\theta^{**} = \theta^p \exp \left(-\frac{\Delta t}{2L}(V^n + V^{**}) \right) + \frac{2L}{(V^n + V^{**})} \left(1 - \exp \left(-\frac{\Delta t}{2L}(V^n + V^{**}) \right) \right), \quad (51)$$

468 and from equation (23) $\langle \phi \rangle_{pl}^{**}$ is computed using θ^{**} .

469 8. Updating p_c : for the sake of brevity, we will only refer to the code (Heimisson, 2022),
 470 see also data availability statement, for a detailed implementation of this time-
 471 step, but a summary follows. In equation (24) (after substituting with equation
 472 (14) for $\langle p \rangle$) we approximate the $\partial^2/\partial x^2$ derivative with second-order finite dif-
 473 ference approximation. The time-integral is discretized using a trapezoidal rule.
 474 Predictions from step 1 and 3 are used to compute the various fields at time t^{n+1}
 475 except we solve for p_c^{**} (the prediction of p_c for time t^{n+1}) implicitly by solving
 476 a system of linear equations.

477 9. Finally p_c^{**} is used to update δ_y^{**} , $\langle p \rangle^{**}$, and $\delta_x^{**} = \delta_x^n + \Delta t(V^n + V^{**})/2$.

478 After the steps above, the algorithm determines if it will proceed to the next time-
 479 step or reiterate following these rules.

- 480 • A minimum of one iteration is used. If the algorithm finishes the aforementioned
 481 steps for the first time at the current time then it must iterate again. The algo-
 482 rithm moves back to step 1, but instead of explicit guesses for the new time step
 483 it uses previous updates. That is $\delta_x^{**} \rightarrow \delta_x^*$, $\delta_y^{**} \rightarrow \delta_y^*$, and $p_c^{**} \rightarrow p_c^*$.
- 484 • If a minimum one iteration has been done, the algorithm checks for absolute and
 485 relative error in the estimate of p_c . That is if $\max(|p_c^{**} - p_c^*|)/(a\sigma_0) > \xi/10$ (where
 486 a is the direct effect parameter) or $\|p_c^{**} - p_c^*\|_1/\|p_c^*\|_1 > \xi/10$ is violated then a
 487 new time-step is selected $\Delta t \rightarrow \Delta t/2$ and the algorithm proceeds to step 1 us-
 488 ing the following initial predictions $(\delta_x^{**} + \delta_x^n)/2 \rightarrow \delta_x^*$, $(\delta_y^{**} + \delta_y^n)/2 \rightarrow \delta_y^*$, and
 489 $(p_c^{**} + p_c^n)/2 \rightarrow p_c^*$. Here ξ is a factor that controls the accuracy of the solution,
 490 in simulations shown later this is set to $\xi = 1/32$, see Appendix B for more dis-
 491 cussion of ξ .
- 492 • If both a minimum of one iteration has been carried out and the error tolerances
 493 are satisfied, the algorithm proceeds to a new time step and ** predictions are as-

494 signed as field values are time t^{n+1} . Finally, the new initial time-step is selected
 495 $\Delta t \rightarrow \min(\xi V^{n+1}/L, 1.1 \cdot \Delta t)$ where first we make sure that the state evolution
 496 is well resolved, by picking ξ sufficiently small. Second, we make sure not to grow
 497 the time-step too much if the pore pressure evolution requires a smaller time-step
 498 than indicated by $\xi V^{n+1}/L$.

499 **4.3 Convolution kernel computation and truncation**

500 Alongside with the time stepping, which was described in the previous section, we
 501 update and calculate the convolution in equations (44), (46), and (47). In computing the
 502 convolution we first compute a kernel values at lag times t_i for each wavenumber k_n i.e.
 503 $K_1(t_i, k_n)$ and $K_2(t_i, k_n)$, where t_i is selected to span a time interval from $\zeta_l \min(t_b, t_f)$
 504 to $\zeta_u \min(t_b, t_f)$. In practice we take $\zeta_l = 10^{-6}$ and $\zeta_u = 20$ and t_b and t_f are the dif-
 505 fusion time-scales of the bulk and of the flux through the shear zone:

$$t_b = \frac{1}{ck^2}, \tag{52}$$

506 and

$$t_f = \frac{1}{\mathcal{F}^2 ck^2} = \frac{\kappa^2 \epsilon^2}{\kappa_c^2 c}. \tag{53}$$

507 We thus evaluate the convolution kernels between a time that is negligible com-
 508 pared to the diffusional time-scales $\zeta_l \min(t_b, t_f)$, up to a time that is long compared to
 509 the diffusional time scales $\zeta_u \min(t_b, t_f)$. Evaluation points t_i are selected by combining
 510 both points at a linearly equally spaced times, and logarithmically equally spaced times.
 511 Here we use 1024 evaluation points, but we found for in some cases, such as the bench-
 512 marking against the linear stability analysis of Heimisson et al. (2021) that much fewer
 513 evaluation points were needed.

514 Since we pre-compute the convolution kernels we need to determine the values of
 515 the Fourier coefficients $D_{x,n}$, $D_{y,n}$, P_n at times $t-t_i$. This is done by storing the Fourier
 516 coefficients' values at selected times and then determining their values at the convolu-
 517 tion times t_i by linear interpolation.

518 The criteria for storing a Fourier coefficient value are implemented by setting an
 519 integer N_{st} , which is the maximum number of time-steps that can be taken without stor-
 520 ing the Fourier coefficients. We compute

$$N_{st} = \lfloor \min(1 + \min(t_f, t_b)/\Delta t; 1 + \min(a\sigma_0/(p_c^n - p_c^{lst}))/20; N_{st}^{\max}) \rfloor, \quad (54)$$

521 where p_c^{lst} is the vector of p_c values when the Fourier coefficients were last stored and
 522 N_{st}^{\max} is some user-determined value that makes sure the coefficients are sampled at least
 523 every N_{st}^{\max} time-step. The first criterion in the equation makes sure that the minimum
 524 diffusion time is resolved in the stored Fourier coefficients and thus changes the Fourier
 525 coefficients that occur on time scales relevant for diffusion are stored. Testing has sug-
 526 gested that under-sampling here may not be an issue since the shortest diffusion times
 527 correspond to the largest wavenumbers (shortest wavelengths) and if the simulation is
 528 well resolved, then the influence of these wavelengths is negligible. The second criterion
 529 makes sure that if the pore pressure is changing rapidly, then information of these rapid
 530 changes is stored in the stored coefficients. This is particularly important for injection
 531 problems. However, for efficiency we overwrite the value above for N_{st} if $t^n - t^{lst} < \zeta_I \min(t_b, t_f)$,
 532 where t^{lst} is the time when the coefficients were last stored, in which case we set $N_{st} =$
 533 N_{st}^{\max} . This makes sure that we do not store coefficients over time scales too short for
 534 any diffusional process to occur. This makes the seismic phase of the simulations much
 535 more efficient.

536 5 Application

537 Here we show an application of the code. We compare the code to the Guglielmi
 538 et al. (2015) experiment, in which fluid was injected into a shallow fault and slip and pres-
 539 sure were monitored. The slip and pressure data was previously analyzed by Larochelle
 540 et al. (2021a) by modeling 1D diffusion in a plane strain linear elastic bulk with rate-
 541 and-state friction. We use their parameter estimates (see also table A1) and their sim-
 542 plified pore pressure history (see Figure 2 in Larochelle et al., 2021a) as input, but we
 543 vary other processes and parameters that were not accounted for by Larochelle et al. (2021a),
 544 or in most comparable studies, such as dilatancy, different permeabilities of the bulk com-
 545 pared to the shear zone, and poroelastic parameters. Specifically, we explore a set of pa-
 546 rameters where the dilatancy coefficient takes values $\gamma = 0$, $1.7 \cdot 10^{-5}$, and $1.7 \cdot 10^{-4}$. Fur-
 547 ther, the bulk hydraulic diffusivity is $c = 4 \cdot 10^{-8}$ or $4 \cdot 10^{-7}$ m²/s and the undrained Pois-

548 son's ratio is $\nu = 0.35$ or 0.262 . We note further discussion of parameters in Appendix
 549 A.

550 We follow the setup and initial conditions as implemented by Laroche et al. (2021a).
 551 However, some critical differences in model setup and characterization of fluid flow are
 552 worth mentioning. Laroche et al. (2021a) implement 1D isotropic diffusion, meaning
 553 the pressure in the bulk and shear zone is spatially constant in y , and no fluid-solid cou-
 554 pling of the bulk. This implies isotropic diffusivity across the shear zone and bulk and
 555 that the bulk is purely elastic, thus no coupling of fluid flow and deformation. Here we
 556 can create an elastic bulk response by selecting the hydraulic diffusivity as either very
 557 large or very small (drained and undrained conditions, respectively). However, this would
 558 make the bulk extremely diffusive or impermeable, which is then inconsistent with Laroche
 559 et al. (2021a) where bulk diffusion is relevant at the time scale of nucleation. This in-
 560 compatibility, along with some other critical differences, makes the direct comparison
 561 of results most likely impossible. Here we assume that the pressure measured in the ex-
 562 periment Guglielmi et al. (2015) reflects the shear zone center pressure p_c , whereas in
 563 Laroche et al. (2021a) this would be a constant value along the y -dimension at $x =$
 564 0.

565 We stress that the goal here is neither to replicate the simulations and results Laroche
 566 et al. (2021a) nor to model the experiments of Guglielmi et al. (2015) explicitly. Here
 567 the goal is to use these previous results to guide us in finding the approximately right
 568 part of the parameter space and be consistent with experimental values. Then we wish
 569 to vary other properties that are generally not tested in comparable studies to under-
 570 stand if they significantly affect the slip process and nucleation during injection.

571 **5.1 Reference case, no dilatancy**

572 First, we explore the simplest case, and the one most studied in the literature, where
 573 pore pressure change in the shear zone is introduced only by injection and does not cause
 574 pressure change through dilatancy. In most cases, this would mean that the pore pres-
 575 sure change is one-way coupled. In other words, the pore pressure changes slip by affect-
 576 ing the frictional strength, but the slip does not change the pore pressure (e.g. Bhattacharya
 577 & Viesca, 2019; Cappa et al., 2019; Laroche et al., 2021a). However, in our case, this
 578 is not true due to the poroelastic coupling. For example, the fault pressurization changes

579 δ_y , which causes compaction of the host rock and this changes pore pressure adjacent
 580 to the shear zone.

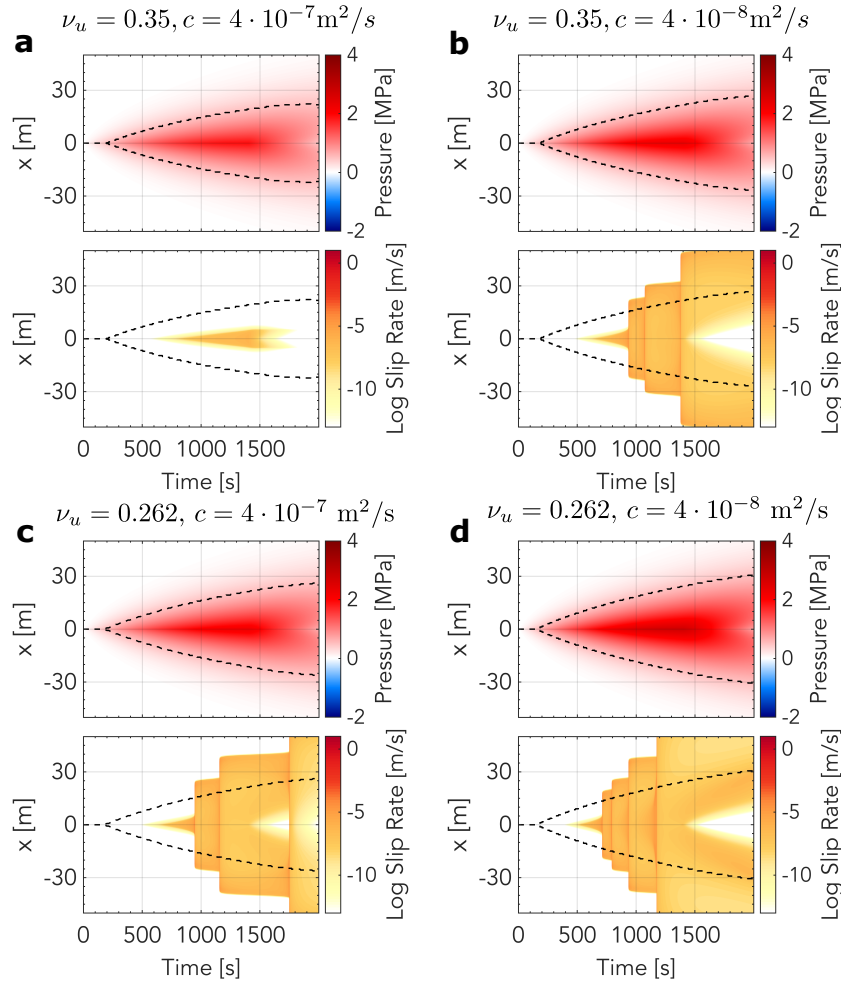


Figure 3. Simulations of fault fields with time and no dilatancy $\gamma = 0$ but varied bulk diffusivity c and undrained Poisson's ratio ν_u as is listed above each panel. Each panel shows the average shear zone pressure $\langle p \rangle$ and log slip rate $\log_{10} V$. x indicates location along the length of the fault, but we note that the simulation domain is 5 times larger (400 m) than is shown. The black dashed lines are the 0.5 MPa pressure contours, which we take as representative of the pressure front distance. We observe highly stabilized slip in panel **a**, where the undrained Poisson's ratio and the bulk diffusivity are larger. However, highly unstable slip in panel **d** with a smaller undrained Poisson's ratio and bulk diffusivity (four seismic events).

581 The simulations without dilatancy (Figure 3) demonstrate a wide spectrum of slip
 582 stability based on two parameters that have not been explored much in the literature:
 583 bulk diffusivity and undrained Poisson’s ratio. First, with larger bulk diffusivity c and
 584 undrained Poisson’s ratio ν_u (panel **a**) we observe very limited slip in response to the
 585 injection. Clearly, the fault is not slipping in a seismically unstable manner. In contrast,
 586 a smaller undrained Poisson’s ratio ν_u and bulk diffusivity c (panel **d**) result in highly
 587 unstable behavior with four seismic ruptures. In the two other cases, where one value
 588 is larger and the other smaller (panels **b** and **c**), we see similarly unstable behavior with
 589 three ruptures. This may indicate a degree of trade-off between ν_u and c , and neither
 590 parameter alone is controlling the stability characteristics of the fault. This makes sense
 591 since c will control the slip speed at which the bulk will respond in an undrained man-
 592 ner. We discuss how the undrained parameters play a significant role in the stability in
 593 section 6.1.

594 **5.2 Simulations with dilatancy $\gamma = 1.7 \cdot 10^{-5}$**

595 Here we explore the same parameter combinations, initial conditions, imposed in-
 596 jection, and overall setup as in Figure 3. However, we now include dilatancy setting $\gamma =$
 597 $1.7 \cdot 10^{-5}$. This is 10% of the standard value of $\gamma = 1.7 \cdot 10^{-4}$, which Segall and Rice
 598 (1995) derived from the experiments of Marone et al. (1990). $\gamma = 1.7 \cdot 10^{-4}$ is typi-
 599 cally used in the literature and results using that value will be shown in the next sec-
 600 tion. However, we decided to explore a smaller value as it reveals an intermediate regime
 601 where slow slip outpaces the diffusion front (Figure 4)

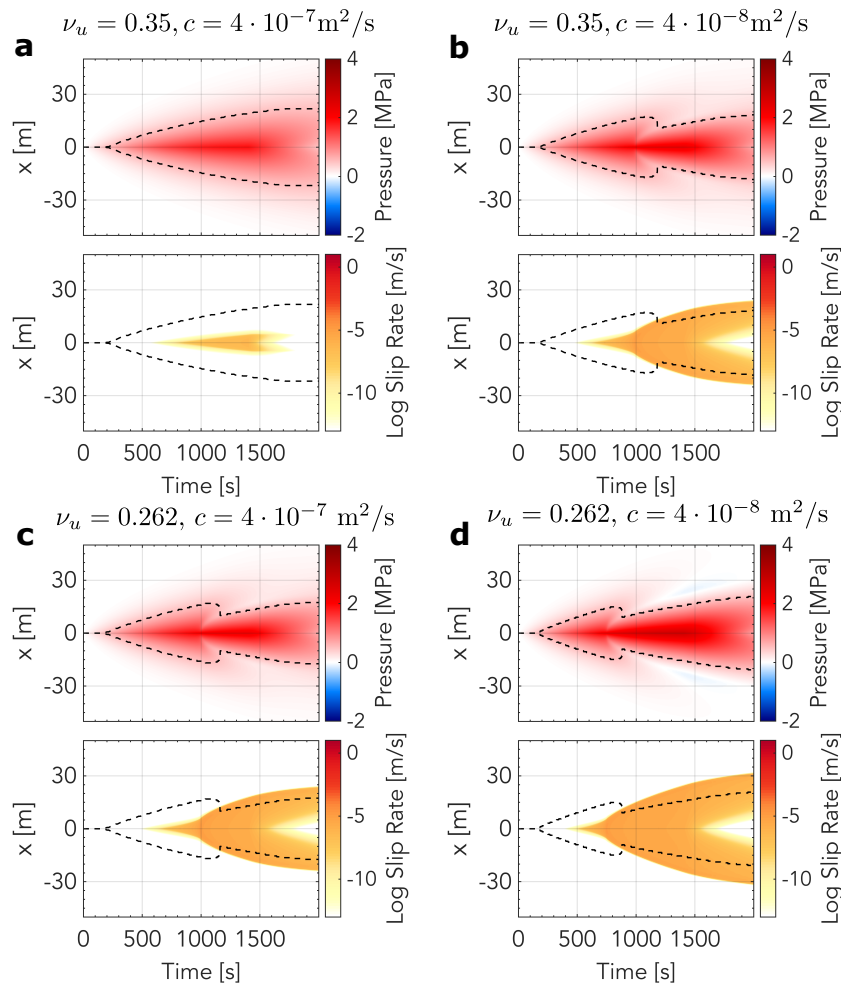


Figure 4. Simulations of fault fields with time and dilatancy $\gamma = 1.7 \cdot 10^{-5}$. Otherwise, the figures and simulation setup are the same as in Figure 3. We observe highly stabilized slip in panel a, where the undrained Poisson's ratio and the bulk diffusivity are larger. Here the results are largely consistent with those of Figure 3 where panel a shows very stable behavior, panel d is the most unstable, and parameter combinations in panels b and c show similar stability. However, here all simulations show gradual migration of a slow slip front and no seismic event. Thus all simulations are substantially stabilized, as is expected from introducing dilatancy. We note negative pore pressure change at the slip-front in panel d, and strong overall deviation from the square root characteristic growth of the pore pressure front.

602 It is notable in Figure 4 that we observe similar effect of stabilization by chang-
 603 ing c and ν_u compared to Figure 3, with larger ν_u and c showing high degree of stabi-
 604 lization (panel a), but smaller ν_u and c a developing instability, but panels b and c have

605 similar levels of stability. However, in Figure 4 the style of slip is very different. We ob-
 606 serve no seismic events but slow slip migration. In all cases, except panel a, the slow slip
 607 outpaces the pore pressure front as indicated by the dashed 0.5 MPa contour. At the same
 608 time, the slip is drastically altering the pore pressure front. The influence of dilatancy
 609 on the fault pore pressure is most prominent in panel d, where the average pressure at
 610 the rupture tip is decreased compared to a background value, i.e. negative pore pressure
 611 change. The result is not a classic square-root-of-time diffusional pressure characteris-
 612 tic as is seen in Figure 3 and Figure 4a but rather square-root characteristic initially, but
 613 once the slip speed is significant and the dilatancy alters the pore pressure and the char-
 614 acteristic is perturbed. The resulting shape of the fault pore pressure contour resembles
 615 the outline of a squid’s head.

616 **5.3 Simulations with dilatancy $\gamma = 1.7 \cdot 10^{-4}$**

617 Finally, we carry out simulations using the value of the dilatancy coefficient $\gamma =$
 618 $1.7 \cdot 10^{-4}$ as inferred by Segall and Rice (1995). This may be considered as a standard
 619 value as it is typically used. However, there is no general reason to believe that the di-
 620 latancy coefficient could not vary significantly.

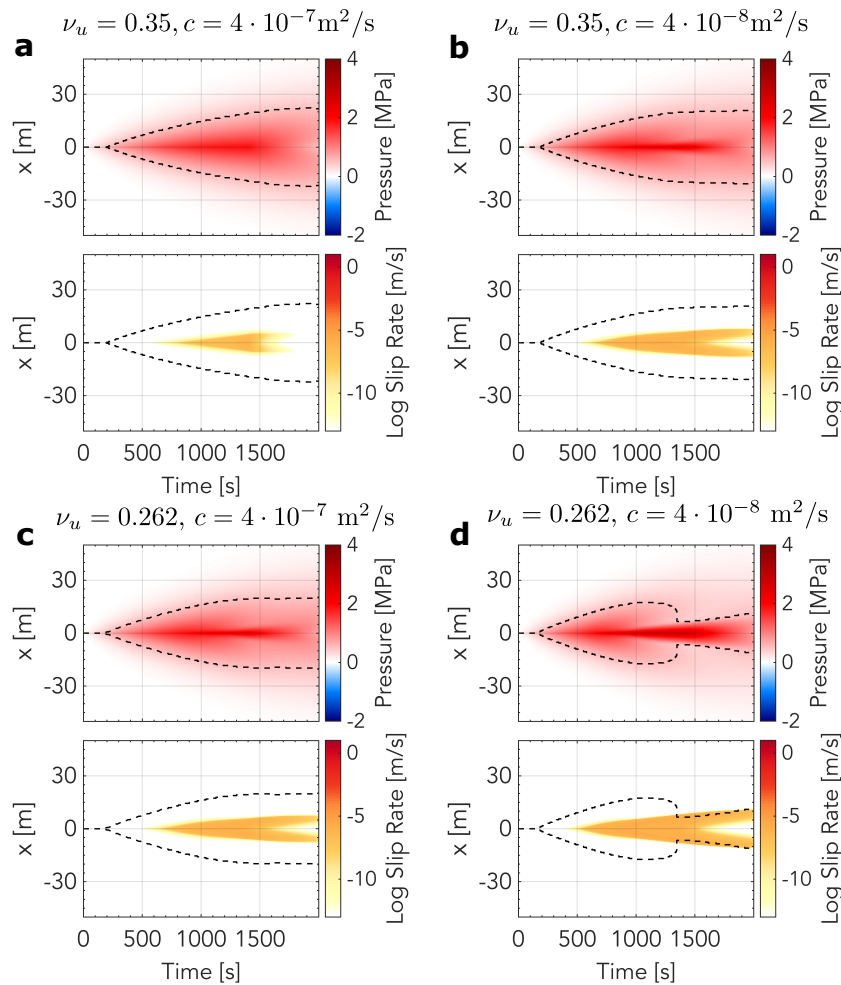


Figure 5. Simulations of fault fields with time and dilatancy $\gamma = 1.7 \cdot 10^{-4}$. Otherwise the figures and simulation setup is the same as in Figure 3. We observe highly stabilized slip in all cases. Unlike the previous two cases the rupture only grows in a region of significantly elevated pore pressure.

621 For $\gamma = 1.7 \cdot 10^{-4}$ we observe highly stabilized slip (Figure 5). There is no seis-
 622 mic rupture and no slow slip front that is growing faster than the pore pressure diffuses.
 623 In other words, the rupture is driven in the location of high pore pressure and thus grows
 624 quasi-statically with the pressure front. Dilatancy influences the fault pressure, in par-
 625 ticular in Figure 5d, but compared to Figure 4 we observe that the dilatancy induced
 626 changes in pore pressure are less prominent in Figure 5. This may be somewhat coun-
 627 terintuitive given that the dilatancy coefficient is an order of magnitude larger in Fig-
 628 ure 5. Since the dilatancy coefficient is smaller in Figure 4 a larger slip patch can de-

629 velop before dilatancy becomes significant. This slip patch is less stiff or alternatively
630 one might state that it produces a higher energy release rate. Thus it is able to drive rup-
631 ture propagation at a higher rate and more slip speed, which ultimately results in increased
632 pore pressure response than when the dilatancy coefficient is larger and suppresses in-
633 stability development at an earlier time. We emphasize that selecting $\gamma = 1.7 \cdot 10^{-4}$
634 does not generally mean stable rupture due to injection. Even if all the same parame-
635 ters are selected, a seismic rupture could develop by simply altering the injection strat-
636 egy; for example, injecting for a significantly longer time and at a higher rate would likely
637 eventually lead to a seismic event.

638 **6 Discussion**

639 **6.1 Result summary and interpretation**

640 The application of our method has had two main themes. First, by exploring how
641 dilatancy affects the fault response due to injection. Second, how altering the bulk dif-
642 fusivity and undrained Poisson's ratio influences the fault response from injection. Di-
643 latancy is already understood to be a stabilizing mechanism (Rudnicki & Chen, 1988;
644 Segall & Rice, 1995; Segall et al., 2010), although limited study of coupled injection and
645 dilatancy has been carried out (except Ciardo & Lecampion, 2019; Yang & Dunham, 2021).
646 Thus our general finding, that fault slip is stabilized and aseismic slip is promoted when
647 dilatancy is included is not surprising. We have thus chosen to contrast this well-known
648 stabilizing mechanism with less explored parameters that we are uniquely positioned to
649 investigate with the method described in this paper. Namely we vary parameters c and
650 ν_u . Indeed the latter has meaning only for a poroelastic solid. A purely elastic solid, as
651 considered in most studies (with some exceptions, e.g. Jha & Juanes, 2014; Torbernts-
652 son et al., 2018; Heimisson et al., 2019) has only a single Poisson's ratio.

653 Our selection of three different γ values reveals different modes of rupture. First,
654 highly unstable response with repeated seismic ruptures of the same part of the fault.
655 Second, slow slip migration that propagates beyond the pressurized region. Finally, quasi-
656 statically growing slip only in regions of high pressure. This can be observed in Figures
657 3, 4, and 5 respectively. The Guglielmi et al. (2015) experiment reported primarily aseis-
658 mic slip and significant dilatant behavior. Some micro-earthquakes were reported, but
659 they may have been off the main fault and represent only a small fraction of the moment

660 released. Thus our findings show, given the experimental constraints and information
661 from a previous modeling study (Larochelle et al., 2021a) that inclusion of dilatancy re-
662 sults in behavior qualitatively similar to what was reported by Guglielmi et al. (2015).
663 However, further study is needed for quantitative matching. We highlight that the method
664 presented predicts fault opening from dilatancy or pressurization and thus may provide
665 additional constraints in data application when that is directly measured (Cappa et al.,
666 2019).

667 Our reported influence of bulk diffusivity and undrained Poisson's ratio is more novel.
668 We observe that changing the bulk diffusivity by order of magnitude significantly sta-
669 bilizes the fault in the simulations. It is important to emphasize that this result is also
670 contingent on the shear zone mobility, which we have not systematically varied. This is
671 due to the time scales of fluid diffusion in the bulk and shear zone are not independent
672 as discussed by Heimisson et al. (2021). The bulk diffusivity has an important control
673 on the stability of the fault as it will control how rapidly fluids can escape the shear zone.
674 Our parameter choice (Appendix A) is such that it reflects a fault initially far from steady-
675 state or, in other words, not critically stressed. Although the changes in average pres-
676 sure in Figures 3, 4, and 5 are subtle, they are sufficient to cause significant stabiliza-
677 tion in fault behavior. This can be observed by comparing panels **a** and **b**, or **c** and **d**
678 in Figures 3, 4, and 5.

679 Bulk diffusivity is often considered to be the same as that of the shear zone or the
680 bulk is simply taken to be impermeable. In this study, we have taken what we consider
681 to be small values of c , yet we observe a very significant effect. Further, as seen in equa-
682 tion (22) the flux into the bulk scales with κ_{cy}/ϵ^2 . Since we expect ϵ the shear zone half-
683 thickness to be small, we can expect that flux into the bulk occurs rapidly. Indeed in this
684 study, we set the κ_{cx} , along shear zone mobility, to be a factor 10^9 larger than κ_{cy} such
685 that the fluid migration along the shear zone was significant compared to the flux into
686 the bulk. This highlights that how rapidly the bulk can transport fluids is critical for the
687 fault dynamics. As discussed in Heimisson et al. (2021), and can be seen in the SBI so-
688 lutions in this paper, the characteristic time of bulk diffusion is $\sim 1/(ck^2)$. Thus the bulk
689 fluid transport is highly dependent on length scale, and idealizations of an impermeable
690 bulk may only be valid at a certain length scale.

691 The dependence on the undrained Poisson's ratio may be surprising, and it may
 692 not be clear why having a pronounced undrained poroelastic response will result in a greater
 693 stabilization. The analysis of Heimisson et al. (2021) provides some insight. The undrained
 694 critical wavenumber is

$$|k_{cr}^{un}| \simeq \frac{2\sigma_0(b-a)(1-\nu_u)}{GL} \left(1 - \frac{f_0\gamma}{\beta\sigma_0(b-a)} + \mathcal{O}(\epsilon) \right), \quad (55)$$

695 and the corresponding drained wavenumber is

$$|k_{cr}^d| \simeq \frac{2\sigma_0(b-a)(1-\nu)}{GL} \left(1 - \frac{f_0\gamma}{\beta\sigma_0(b-a)} + \mathcal{O}(\epsilon) \right), \quad (56)$$

696 assuming the shear zone mobility tends to zero. Thus the ratio of the minimum unsta-
 697 ble wavelength in drained and undrained limits is

$$\frac{\lambda_d}{\lambda_{un}} = \frac{1-\nu}{1-\nu_u}, \quad (57)$$

698 Thus, at most, this ratio can be 2, but more commonly around 1 – 1.5. In simple terms,
 699 it means that a perturbation or a slip patch on the fault of length ΔL may be unstable
 700 if the bulk responds in a drained manner. However, the patch or perturbation may need
 701 to be up to $2\Delta L$ to be unstable if the bulk responds in an undrained manner. There are
 702 a few things to note about this stabilization. First, that it depends on the bulk diffu-
 703 sivity, length scale, and slip rate. The transition from a drained to undrained response
 704 will depend on the characteristic bulk diffusion time $\sim 1/(ck^2)$ relative to how fast the
 705 fault is slipping and the slip patch length scale (due to the k^2 dependence). Thus the
 706 timing of stabilization by a transition from drained to undrained response is nontrivial.
 707 Second, the drained and undrained limits are inadequate to characterize the stabiliza-
 708 tion fully. Heimisson et al. (2021) showed that in an intermediate (neither drained nor
 709 undrained) regime, the fault could be more stable than in the undrained regime. Finally,
 710 since anti-plane sliding does not depend on Poisson's ratio, the same kind of stabiliza-
 711 tion will not occur. This may lead to interesting directional effects in 3D simulations.

712 Panels **b** and **c** in Figures 3, 4, and 5 consistently show similar rupture propaga-
 713 tion and stabilization. This suggests that, in a certain sense, that setting $\nu_u = 0.35$ is
 714 approximately equally stabilizing as setting $c = 4 \cdot 10^{-7} \text{ m}^2/\text{s}$ relative to the respec-
 715 tive lower values in the simulation setup. Due to the many complexities mentioned in

716 the previous paragraph we don't think this will hold generally. However, simulations with
 717 combined $\nu_u = 0.35$ and $c = 4 \cdot 10^{-7} \text{ m}^2/\text{s}$ are nearly identical regardless of the γ value
 718 (**a** in Figures 3, 4, and 5). This observation highlights that bulk effects through com-
 719 bined diffusion and poroelasticity can be so stabilizing that dilatancy never becomes sig-
 720 nificant enough to affect the rupture propagation and nucleation.

721 **7 Conclusions**

722 We have presented novel spectral boundary-integral (SBI) solutions applicable to
 723 frictional and fracture mechanics problems in a plane strain linear poroelastic solid. The
 724 solutions consider that the interface of two poroelastic half-spaces may undergo mode
 725 I and II displacement discontinuity as well as pressurization. We have applied the so-
 726 lutions to develop a method and code implementation of a rate-and-state fault that has
 727 simultaneous inelastic dilatancy and injection. We apply this code to data from a field
 728 experiment, which has been previously analyzed by modeling. We explore the role of in-
 729 elastic dilatancy, bulk diffusion, and poroelastic properties of the bulk on the simulation
 730 results. We find, surprisingly, that bulk diffusion and poroelastic properties of the bulk,
 731 which are parameters that are rarely explored, can qualitatively affect rupture stabil-
 732 ity and propagation. Further, we find the stabilization of bulk diffusion and poroelas-
 733 tic properties can be comparable to the well-known stabilizing dilatancy mechanism.

734 **Data Availability Statement**

735 No original data is presented in this study. The data used in regard to application to the
 736 (Guglielmi et al., 2015) field experiment was archived by Larochelle et al. (2021b): Cal-
 737 techDATA repository (<https://data.caltech.edu/records/1891>). The software im-
 738 plementation of the method described in this paper is available here
 739 <https://doi.org/10.5281/zenodo.6010353> (see Heimisson, 2022).

740 **Acknowledgments**

741 This study was supported by the Geophysics Option Postdoctoral Fellowship from the
 742 Division of Geological and Planetary Sciences at Caltech and ETH Postdoctoral fellow-
 743 ship (Project No. FEL-19 20-2) to E.R.H. The work was further supported by the NSF-
 744 IUCRC Center for Geomechanics and Mitigation of Geohazards (projects GMG-4.1, GMG-
 745 4.2) to N.L.

746 **Appendix A Parameter values**

747 Here we briefly explain how the parameter values, listed in the table below, are set.

748 Parameters G , ν , and all friction and loading parameters in Table A1 are from Larochelle
 749 et al. (2021a). Compressibilities $\beta_f^p, \beta_f^\sigma, \beta_n^p, \beta_n^\sigma, \beta_g^p, \beta_g^\sigma$ in addition to ϕ_0 and ϵ are selected
 750 as in Heimisson et al. (2021).

751 Skempton’s coefficient is fixed and set to 0.85, this value is representative of West-
 752 erly granite as well as certain types of sandstone and other rocks. The undrained Pois-
 753 son’s ratio is, on one hand, set to 0.35 to reflect the approximate value of Westerly gran-
 754 ite and on the other hand to 0.262 to represent the undrained value of Charcoal gran-
 755 ite. We note that Charcoal granite has $\nu = 0.270$ and $\nu_u = 0.292$ (Cheng, 2016). How-
 756 ever, we wish to fix ν such that we do have multiple parameters varying each simulation.
 757 Thus only the range $\nu_u - \nu$ is the same as for Charcoal granite albeit the Poisson’s ra-
 758 tios are similar in absolute terms. Further, Charcoal granite has a substantially lower
 759 Skempton’s coefficient $B = 0.454$, but we still use $B = 0.85$ again to limit the num-
 760 ber of varying parameters. We, therefore, do not recommend using this paper as a ref-
 761 erence for poroelastic parameters, but rather look at the overview of Detournay and Cheng
 762 (1995); Cheng (2016), which we used, and references therein for more information on er-
 763 ror and methods for measuring. Here we simply want to explore two cases where $\nu_u -$
 764 ν small and large, but at the same time make sure that the ranges reflect real values mea-
 765 sured in rocks.

766 As explained in the main text, the range of the dilatancy coefficient is selected to
 767 reflect three different styles of ruptures. First we set $\gamma = 0$ and $\gamma = 1.7 \cdot 10^{-4}$ as trial
 768 values where the latter is the standard value used and was identified by Segall and Rice
 769 (1995). We observed that the two values would typically render either highly unstable
 770 or very stable slip. Thus an value of $\gamma = 1.7 \cdot 10^{-5}$ was identified as producing sus-
 771 tained slow slip migration.

772 The two mobilities κ_{cx}, κ_{cy} and the bulk hydraulic diffusivity c were determined
 773 by trial and error by trying to approximately match the pore pressure evolution in Larochelle
 774 et al. (2021a). We highlight that due to the heterogeneous permeability structure, the
 775 fact that we treat the pore pressure as non-constant in the shear zone, and other cou-

776 pling mechanisms that alter the pore pressure, we cannot simply select parameters that
 777 give exactly the same pore pressure evolution as in Larochelle et al. (2021a).

778 **Appendix B Method validation**

779 The spectral boundary-integral method, in addition to the rate-and-state fault slip
 780 simulations, couples together several physical processes that could not be simulated with
 781 another individual code. Further, no analytical solutions are available that also couple
 782 all these processes. It is, therefore, nearly impossible to benchmark and test all capa-
 783 bilities of the code and implementation simultaneously. However, here we list to provide
 784 an overview of the tests and validation we carried out.

- 785 • As was reported in Figure 2 the SBI solutions for τ' and p^\pm were tested against
 786 the solutions of (Song & Rudnicki, 2017).
- 787 • The analytical inversion of the Laplace transform was in all cases tested by also
 788 numerically inverting the Laplace transform numerically using the Talbot method
 789 (Talbot, 1979)
- 790 • Using p^+ as the relevant pore pressure when computing the effective normal stress,
 791 we reproduced the results of (Heimisson et al., 2019), which were done with a dif-
 792 ferent code (Torberntsson et al., 2018). We, for example, reproduced the sponta-
 793 neously occurring instabilities at mildly rate-strengthening friction that give rise
 794 to slow-slip pulses, which only occur in a limited parameter regime. Our results
 795 were consistent with the spatial dimension of the instabilities and the pulse prop-
 796 agation speeds as reported by (Heimisson et al., 2019).
- 797 • Using the linearized stability analysis of (Heimisson et al., 2021) we identified the
 798 critical wavenumber for many different regimes, such as high diffusivity, low dif-
 799 fusivity, intermediate diffusivity as well as thicker and thinner shear zones. In the
 800 code, a fully non-linear implementation, we induced a critical wavelength pertur-
 801 bation, as determined by the linearized analysis, by introducing a small pertur-
 802 bation in the initial state around steady-state sliding. We found in all cases that
 803 the perturbation in the slip speed oscillated without growing or decaying.

804 The tests and benchmarking above do validate most aspects of the implementa-
 805 tion and method we have introduced in this paper. However, none test the injection into
 806 the fault and fluid propagation as a result of the injection. In order to check the robust-

Table A1. Parameter values in the study

Symbol	Description	Value
<i>Bulk and gouge material properties</i>		
G	Shear modulus	10 GPa
B	Skempton's coefficient	0.85
ν	Drained Poisson's ratio	0.24
ν_u	Undrained Poisson's ratio	0.35, 0.262
$\beta_f^p, \beta_f^\sigma$	Isotropic and uniaxial fluid compressibility	$0.44 \cdot 10^{-9} \text{ Pa}^{-1}$, $0.24 \cdot 10^{-9} \text{ Pa}^{-1}$,
$\beta_n^p, \beta_n^\sigma$	Isotropic and uniaxial pore volume compressibility	$6.0 \cdot 10^{-9} \text{ Pa}^{-1}$, $3.3 \cdot 10^{-9} \text{ Pa}^{-1}$,
$\beta_g^p, \beta_g^\sigma$	Isotropic and uniaxial solid gouge compressibility	$0.020 \cdot 10^{-9} \text{ Pa}^{-1}$, $0.011 \cdot 10^{-9} \text{ Pa}^{-1}$,
ϕ_0	Reference porosity	0.068
γ	Dilatancy coefficient (Segall & Rice, 1995)	0, $1.7 \cdot 10^{-5}$, $1.7 \cdot 10^{-4}$
ϵ	Shear-zone half thickness	1.0 mm
c	Bulk hydraulic diffusivity	$4 \cdot 10^{-8}$, $4 \cdot 10^{-7} \text{ m}^2/\text{s}$
κ_{cx}	Along shear-zone mobility	$8.7584 \cdot 10^{-11} \text{ m}^2/(\text{Pa s})$
κ_{cy}	Across shear-zone mobility	$8.7584 \cdot 10^{-20} \text{ m}^2/(\text{Pa s})$
<i>Friction and loading parameters</i>		
L	Characteristic state evolution distance	16.75 μm
a	Direct rate dependence of friction	0.01125
b	State dependence of friction	0.016
α_{LD}	Linker and Dieterich (1992) constant	0.0
V_0	reference slip rate	10^{-6} m/s
f_0	reference friction	0.55
τ_0	Initial shear stress	2.15 MPa
σ_0	Initial effective normal stress	4 MPa

807 ness of the algorithm in this regard, we set up a problem with injection and delayed nu-
808 cleation with dilatancy. The simulations are run until the slip speed reaches 1 cm/s, which
809 we take as the instability time. This setup thus tests how well the pore pressure injec-
810 tion and subsequent diffusion is resolved as it promotes instability. We generate a man-
811 ufactured solution with the error tolerance and state integration parameter set to $\xi =$
812 $1/4096$ (see section 4.2). Then setting $\xi \in \{1/4, 1/8, 1/16, 1/32, 1/64\}$ and investigat-
813 ing the L_1 norm error of the manufactured solution and the less accurate solutions plot-
814 ted against the total number of iterations (which scales with the computational time)
815 we see a second-order convergence. Where we look at the time of instability, the slip speed
816 profile at the instability time, the p_c value at the instability time, and the slip profile at
817 that time. $\xi = 1/32$ roughly correspond to a relative error of 10^{-3} in all the fields we
818 looked at, but we stress that the magnitude of the relative error depends on the prob-
819 lem and the simulation time. For simulations we favor using $\xi = 1/32$ and one mini-
820 mum iteration (see section 4.2 for discussion on iterations). If smaller values than $\xi =$
821 $1/64$ are compared to the manufactured solution, the convergence gets more complicated
822 but tends to improve to the first order with the iteration number. Using no minimum
823 iteration or 2 minimum iterations also works and gives consistent results. We suggest
824 1 minimum iteration is most efficient in terms of obtaining a stable convergent solution
825 at the fewest total iterations.

826 Finally, we note that Figure 3c demonstrates, by chance, that the simulations are
827 well resolved and accurate. A careful inspection of the figures shows that the last event
828 is not one event but two events nucleating at exactly the same time around $x \approx \pm 30$
829 m and then coalescing. While such a high degree of symmetry is not physically realis-
830 tic, it is a strong indication of well-resolved simulations in time and space, especially when
831 it occurs not at the first simulated event. The same phenomenon also occurs in Figure
832 3b, but it is not as clear.

833 **References**

- 834 Ben-Zion, Y., & Rice, J. R. (1997). Dynamic simulations of slip on a smooth fault in
 835 an elastic solid. *Journal of Geophysical Research: Solid Earth*, *102*(B8), 17771-
 836 17784. doi: <https://doi.org/10.1029/97JB01341>
- 837 Bhattacharya, P., & Viesca, R. C. (2019). Fluid-induced aseismic fault slip out-
 838 paces pore-fluid migration. *Science*, *364*(6439), 464–468. doi: 10.1126/science
 839 .aaw7354
- 840 Bizzarri, A., & Cocco, M. (2006). A thermal pressurization model for the sponta-
 841 neous dynamic rupture propagation on a three-dimensional fault: 1. Method-
 842 ological approach. *Journal of Geophysical Research: Solid Earth*, *111*(B5). doi:
 843 <https://doi.org/10.1029/2005JB003862>
- 844 Bürgmann, R. (2018). The geophysics, geology and mechanics of slow fault slip.
 845 *Earth Planet. Sc. Lett.*, *495*, 112–134.
- 846 Cappa, F., Scuderi, M. M., Collettini, C., Guglielmi, Y., & Avouac, J.-P. (2019).
 847 Stabilization of fault slip by fluid injection in the laboratory and in situ. *Sci-*
 848 *ence Advances*, *5*(3), eaau4065. doi: 10.1126/sciadv.aau4065
- 849 Cheng, A. H.-D. (2016). *Poroelasticity* (Vol. 877). Springer.
- 850 Ciardo, F., & Lecampion, B. (2019). Effect of dilatancy on the transition from
 851 aseismic to seismic slip due to fluid injection in a fault. *Journal of Geophys-*
 852 *ical Research: Solid Earth*, *124*(4), 3724–3743. doi: [https://doi.org/10.1029/](https://doi.org/10.1029/2018JB016636)
 853 [2018JB016636](https://doi.org/10.1029/2018JB016636)
- 854 Dal Zilio, L., Lapusta, N., & Avouac, J.-P. (2020). Unraveling scaling prop-
 855 erties of slow-slip events. *Geophysical Research Letters*, *47*(10). doi:
 856 [10.1029/2020GL087477](https://doi.org/10.1029/2020GL087477)
- 857 Detournay, E., & Cheng, A. H.-D. (1995). Fundamentals of poroelasticity. In *Analy-*
 858 *sis and design methods* (pp. 113–171). Elsevier.
- 859 Dieterich, J. H. (1979). Modeling of rock friction: 1. experimental results and consti-
 860 tutive equations. *Journal of Geophysical Research: Solid Earth*, *84*(B5), 2161-
 861 2168. doi: 10.1029/JB084iB05p02161
- 862 Duchon, C. E. (1979). Lanczos filtering in one and two dimensions. *Journal of ap-*
 863 *plied meteorology*, *18*(8), 1016–1022.
- 864 Dunham, E. M., & Rice, J. R. (2008). Earthquake slip between dissimilar poroelas-
 865 tic materials. *J. Geophys. Res. Solid Earth*, *113*(B9). (B09304) doi: 10.1029/

- 866 2007JB005405
- 867 Ellsworth, W. L. (2013). Injection-induced earthquakes. *Science*, *341*(6142),
868 1225942.
- 869 Guglielmi, Y., Cappa, F., Avouac, J.-P., Henry, P., & Elsworth, D. (2015). Seis-
870 micity triggered by fluid injection-induced aseismic slip. *Science*, *348*(6240),
871 1224–1226. doi: 10.1126/science.aab0476
- 872 Hawthorne, J. C., & Rubin, A. M. (2013). Laterally propagating slow slip events
873 in a rate and state friction model with a velocity-weakening to velocity-
874 strengthening transition. *Journal of Geophysical Research: Solid Earth*,
875 *118*(7), 3785–3808. doi: <https://doi.org/10.1002/jgrb.50261>
- 876 Heimisson, E. R. (2020). Crack to pulse transition and magnitude statistics dur-
877 ing earthquake cycles on a self-similar rough fault. *Earth and Planetary Sci-*
878 *ence Letters*, *537*, 116202. doi: <https://doi.org/10.1016/j.epsl.2020.116202>
- 879 Heimisson, E. R. (2022, February). *eliasrh/poro_sbim: Poro_sbim.v1.0*. Zen-
880 odo. Retrieved from <https://doi.org/10.5281/zenodo.6010353> doi: 10
881 .5281/zenodo.6010353
- 882 Heimisson, E. R., Dunham, E. M., & Almquist, M. (2019). Poroelastic effects
883 destabilize mildly rate-strengthening friction to generate stable slow slip
884 pulses. *Journal of the Mechanics and Physics of Solids*, *130*, 262 – 279. doi:
885 10.1016/j.jmps.2019.06.007
- 886 Heimisson, E. R., Rudnicki, J., & Lapusta, N. (2021). Dilatancy and compaction
887 of a rate-and-state fault in a poroelastic medium: Linearized stability analysis.
888 *Journal of Geophysical Research: Solid Earth*, *126*(8), e2021JB022071. doi:
889 <https://doi.org/10.1029/2021JB022071>
- 890 Hsieh, P. A., & Bredehoeft, J. D. (1981). A reservoir analysis of the denver earth-
891 quakes: A case of induced seismicity. *Journal of Geophysical Research: Solid*
892 *Earth*, *86*(B2), 903–920. doi: <https://doi.org/10.1029/JB086iB02p00903>
- 893 Jha, B., & Juanes, R. (2014). Coupled multiphase flow and poromechanics:
894 A computational model of pore pressure effects on fault slip and earth-
895 quake triggering. *Water Resources Research*, *50*(5), 3776–3808. doi:
896 10.1002/2013WR015175
- 897 Kaneko, Y., Ampuero, J.-P., & Lapusta, N. (2011). Spectral-element simula-
898 tions of long-term fault slip: Effect of low-rigidity layers on earthquake-cycle

- 899 dynamics. *Journal of Geophysical Research: Solid Earth*, 116(B10). doi:
 900 <https://doi.org/10.1029/2011JB008395>
- 901 Lapusta, N., Rice, J. R., Ben-Zion, Y., & Zheng, G. (2000). Elastodynamic analysis
 902 for slow tectonic loading with spontaneous rupture episodes on faults with
 903 rate- and state-dependent friction. *Journal of Geophysical Research: Solid
 904 Earth*, 105(B10), 23765-23789. doi: <https://doi.org/10.1029/2000JB900250>
- 905 Larochele, S., Lapusta, N., Ampuero, J.-P., & Cappa, F. (2021a). Constraining
 906 fault friction and stability with fluid-injection field experiments. *Geophys-
 907 ical Research Letters*, 48(10), e2020GL091188. doi: [https://doi.org/10.1029/
 908 2020GL091188](https://doi.org/10.1029/2020GL091188)
- 909 Larochele, S., Lapusta, N., Ampuero, J.-P., & Cappa, F. (2021b). *Constraining
 910 fault friction and stability with fluid-injection field experiments*. CaltechDATA.
 911 Retrieved from <https://data.caltech.edu/records/1891> doi: 10.22002/D1
 912 .1891
- 913 Leeman, J., Saffer, D., Scuderi, M., & Marone, C. (2016). Laboratory observations
 914 of slow earthquakes and the spectrum of tectonic fault slip modes. *Nature com-
 915 munications*, 7(1), 1–6. doi: <https://doi.org/10.1038/ncomms11104>
- 916 Linker, M. F., & Dieterich, J. H. (1992). Effects of variable normal stress on rock
 917 friction: Observations and constitutive equations. *J. Geophys. Res. Solid
 918 Earth*, 97(B4), 4923–4940. doi: 10.1029/92JB00017
- 919 Liu, Y., & Rice, J. R. (2005). Aseismic slip transients emerge spontaneously
 920 in three-dimensional rate and state modeling of subduction earthquake se-
 921 quences. *Journal of Geophysical Research: Solid Earth*, 110(B8). doi:
 922 <https://doi.org/10.1029/2004JB003424>
- 923 Liu, Y., & Rice, J. R. (2007). Spontaneous and triggered aseismic deformation
 924 transients in a subduction fault model. *Journal of Geophysical Research: Solid
 925 Earth*, 112(B9). doi: <https://doi.org/10.1029/2007JB004930>
- 926 Marone, C. (1998). Laboratory-derived friction laws and their application to seismic
 927 faulting. *Annu. Rev. Earth Pl. Sc.*, 26(1), 643–696.
- 928 Marone, C., Raleigh, C. B., & Scholz, C. H. (1990). Frictional behavior and con-
 929 stitutive modeling of simulated fault gouge. *Journal of Geophysical Research:
 930 Solid Earth*, 95(B5), 7007-7025. doi: 10.1029/JB095iB05p07007
- 931 McNamee, J., & Gibson, R. E. (1960). Plane strain and axially symmetric problems

- 932 of the consolidation of a semi-infinite clay stratum. *Q. J. Mech. Appl. Math.*,
 933 *13*(2), 210–227.
- 934 Noda, H., & Lapusta, N. (2013). Stable creeping fault segments can become de-
 935 structive as a result of dynamic weakening. *Nature*, *493*(7433), 518–521. doi:
 936 <https://doi.org/10.1038/nature11703>
- 937 Proctor, B., Lockner, D. A., Kilgore, B. D., Mitchell, T. M., & Beeler, N. M. (2020).
 938 Direct evidence for fluid pressure, dilatancy, and compaction affecting slip in
 939 isolated faults. *Geophysical Research Letters*, *47*(16), e2019GL086767. doi:
 940 10.1029/2019GL086767
- 941 Raleigh, C., Healy, J., & Bredehoeft, J. (1976). An experiment in earthquake control
 942 at Rangely, Colorado. *Science*, *191*(4233), 1230–1237. doi: 10.1126/science.191
 943 .4233.1230
- 944 Rice, J. R. (2006). Heating and weakening of faults during earthquake slip. *Journal*
 945 *of Geophysical Research: Solid Earth*, *111*(B5). doi: 10.1029/2005JB004006
- 946 Rice, J. R., & Ben-Zion, Y. (1996). Slip complexity in earthquake fault models. *Pro-*
 947 *ceedings of the National Academy of Sciences*, *93*(9), 3811–3818. doi: 10.1073/
 948 pnas.93.9.3811
- 949 Rice, J. R., & Cleary, M. P. (1976). Some basic stress diffusion solutions for fluid-
 950 saturated elastic porous media with compressible constituents. *Rev. Geophys.*,
 951 *14*(2), 227–241. doi: 10.1029/RG014i002p00227
- 952 Rudnicki, J. W., & Chen, C.-H. (1988). Stabilization of rapid frictional slip on a
 953 weakening fault by dilatant hardening. *Journal of Geophysical Research: Solid*
 954 *Earth*, *93*(B5), 4745–4757. doi: 10.1029/JB093iB05p04745
- 955 Rudnicki, J. W., & Koutsibelas, D. A. (1991). Steady propagation of plane strain
 956 shear cracks on an impermeable plane in an elastic diffusive solid. *Int. J.*
 957 *Solids Struct.*, *27*(2), 205–225.
- 958 Rudnicki, J. W., & Rice, J. R. (2006). Effective normal stress alteration due to
 959 pore pressure changes induced by dynamic slip propagation on a plane be-
 960 tween dissimilar materials. *J. Geophys. Res. Solid Earth*, *111*(B10). doi:
 961 10.1029/2006JB004396
- 962 Ruina, A. (1983). Slip instability and state variable friction laws. *Jour-*
 963 *nal of Geophysical Research: Solid Earth*, *88*(B12), 10359–10370. doi:
 964 10.1029/JB088iB12p10359

- 965 Segall, P. (2010). *Earthquake and volcano deformation*. Princeton University Press.
- 966 Segall, P., & Lu, S. (2015). Injection-induced seismicity: Poroelastic and earthquake
967 nucleation effects. *J. Geophys. Res. Solid Earth*, *120*(7), 5082–5103.
- 968 Segall, P., & Rice, J. R. (1995). Dilatancy, compaction, and slip instability of a
969 fluid-infiltrated fault. *Journal of Geophysical Research: Solid Earth*, *100*(B11),
970 22155–22171. doi: 10.1029/95JB02403
- 971 Segall, P., & Rice, J. R. (2006). Does shear heating of pore fluid contribute to earth-
972 quake nucleation? *Journal of Geophysical Research: Solid Earth*, *111*(B9). doi:
973 <https://doi.org/10.1029/2005JB004129>
- 974 Segall, P., Rubin, A. M., Bradley, A. M., & Rice, J. R. (2010). Dilatant strength-
975 ening as a mechanism for slow slip events. *J. Geophys. Res. Solid Earth*,
976 *115*(B12).
- 977 Shibazaki, B., & Shimamoto, T. (2007, 10). Modelling of short-interval silent slip
978 events in deeper subduction interfaces considering the frictional properties at
979 the unstable—stable transition regime. *Geophysical Journal International*,
980 *171*(1), 191–205. doi: 10.1111/j.1365-246X.2007.03434.x
- 981 Song, Y., & Rudnicki, J. W. (2017). Plane-strain shear dislocation on a leaky plane
982 in a poroelastic solid. *J. Appl. Mech.*, *84*(2), 021008.
- 983 Talbot, A. (1979, 01). The Accurate Numerical Inversion of Laplace Transforms.
984 *IMA Journal of Applied Mathematics*, *23*(1), 97–120. doi: 10.1093/imamat/23
985 .1.97
- 986 Tong, X., & Lavier, L. L. (2018). Simulation of slip transients and earthquakes in fi-
987 nite thickness shear zones with a plastic formulation. *Nature communications*,
988 *9*(1), 1–8. doi: <https://doi.org/10.1038/s41467-018-06390-z>
- 989 Torberntsson, K., Stiernström, V., Mattsson, K., & Dunham, E. M. (2018, Jul 19).
990 A finite difference method for earthquake sequences in poroelastic solids. *Com-
991 putat. Geosci.*, *22*(5), 1351–1370. doi: 10.1007/s10596-018-9757-1
- 992 Verruijt, A. (1971). Displacement functions in the theory of consolidation or in ther-
993 moelasticity. *Zeitschrift für angewandte Mathematik und Physik ZAMP*, *22*(5),
994 891–898.
- 995 Viesca, R. C., & Dublanche, P. (2019). The slow slip of viscous faults. *Journal of
996 Geophysical Research: Solid Earth*, *124*(5), 4959–4983. doi: [https://doi.org/10
997 .1029/2018JB016294](https://doi.org/10.1029/2018JB016294)

- 998 Wibberley, C. A., & Shimamoto, T. (2003). Internal structure and permeability
 999 of major strike-slip fault zones: the Median Tectonic Line in Mie Prefecture,
 1000 Southwest Japan. *J. Struct. Geol.*, *25*(1), 59–78.
- 1001 Yang, Y., & Dunham, E. M. (2021). Effect of porosity and permeability evolution on
 1002 injection-induced aseismic slip. *Journal of Geophysical Research: Solid Earth*,
 1003 *126*(7), e2020JB021258. doi: <https://doi.org/10.1029/2020JB021258>
- 1004 Yehya, A., Yang, Z., & Rice, J. R. (2018). Effect of fault architecture and permeabil-
 1005 ity evolution on response to fluid injection. *Journal of Geophysical Research:*
 1006 *Solid Earth*, *123*(11), 9982-9997. doi: <https://doi.org/10.1029/2018JB016550>
- 1007 Zhang, S., Tullis, T. E., & Scruggs, V. J. (1999). Permeability anisotropy and pres-
 1008 sure dependency of permeability in experimentally sheared gouge materials.
 1009 *Journal of Structural Geology*, *21*(7), 795-806. doi: [https://doi.org/10.1016/](https://doi.org/10.1016/S0191-8141(99)00080-2)
 1010 [S0191-8141\(99\)00080-2](https://doi.org/10.1016/S0191-8141(99)00080-2)